# Resonant inelastic x-ray scattering studies of elementary excitations

Ament, L.J.P.

# Chapter 4

# Magnetic RIXS on 2D cuprates

## 4.1 Introduction

Over the past three years, RIXS has made tremendous progress in probing magnetic excitations. From the 3D material NiO via the 2D high-$T_c$ superconductors to the 1D telephone number compounds, many materials have been studied with RIXS. What used to be the exlusive domain of neutron scattering, and to lesser degree Raman spectroscopy and optical conductivity measurements, now is being entered by RIXS.

Neutron scattering measures the dispersion, or, more generally, the dynamic spin susceptibility $\chi(\mathbf{q}, \omega)$ of magnetic compounds with a very high energy resolution (down to the $\mu$eV range [68]). Neutrons, however, have a number of intrinsic difficulties: they require large samples or very high flux, especially at high energy transfers. Some elements are intrinsically unsuitable for neutron scattering because they strongly absorb neutrons (*e.g.*, cadmium and gadolinium [68]).

RIXS does not suffer from these limitations. The energy resolution of RIXS experiments has improved dramatically over the last few years, allowing for the measurement of low energy magnetic excitations down to $\sim 50$ meV. This brings the high-$T_c$ cuprates into the domain of magnetic RIXS, and this will be the main subject of this chapter.

Because of the very rapid developments in instrumentation, theory has trouble keeping up with experiments. Magnetic RIXS measurements on the 2D cuprates have been done at the Cu K edge [14, 53], L edge [10, 11, 21, 69], M edge [15] and O K edge [70, 71].

In the scattering process, angular momentum can be transferred to the solid. RIXS is not restricted to $\Delta S = 0, 1$ like neutrons, which carry spin $1/2$, but can also transfer two units of angular momentum since photons have spin 1. Photons couple only very weakly to the spin angular momentum of the electron. Rather, the photon's angular momentum is transferred to the orbital angular momentum of the electron. This might seem a problem for creating magnetic excitations with X-rays, because in most solids the relativistic spin-orbit coupling is small.

However, for some core states involved in RIXS, the spin-orbit coupling is very large (of the order of 10 eV). Consequently, the spin and orbital degrees of freedom are coupled, so the photon's angular momentum can be transferred indirectly to the spins, creating a magnetic excitation with $\Delta S^z = \pm 1$ or $\pm 2$. This channel is direct RIXS: the final state can be reached without any dynamics in the intermediate state.

1s core states have no orbital angular momentum, and therefore magnetic excitations with $\Delta S^z = \pm 1$ or $\pm 2$ cannot be created at the K edges. However, it is possible to induce a $\Delta S^z = 0$ magnetic excitation, like in two-magnon Raman scattering in the cuprates. This process can arise because the RIXS process creates a magnetic impurity in the intermediate state, which is then screened by the surrounding valence electrons: the magnetic background is rearranged around the core hole site, and left behind in an excited final state. Note that indirect processes can also play a role at edges where there is strong core state spin-orbit coupling (and hence direct RIXS); the indirect RIXS spectral weight will be of sub-leading order, however.

Sec. 4.4 deals with indirect RIXS at the transition metal K edge, where the 1s core hole couples to the spin degree of freedom by locally modifying the superexchange interactions [14, 51–53]. In such a process, the total spin of the valence electrons is conserved, and only excitations where at least two spins are flipped (with total $\Delta S^z = 0$) are allowed. A similar indirect process can also occur at the oxygen K edge [70, 71], see Sec. 4.7.

The first theoretical work on magnetic excitations was done by De Groot *et al.* [72]. They studied $Ni^{2+}$ and $Cu^{2+}$ numerically, and showed that there are no pure spin flips present for a $Cu^{2+}$ ion when the spin is aligned along the $z$ axis and the hole occupies the $3d_{x^2-y^2}$ orbital in a $D_{4h}$ crystal field, see also Ref. [73]. Instead, they predict spin flips accompanying dd excitations. In Sec. 4.5 it will be shown that spin flips are possible when the spin is in the $xy$ plane, and that the resulting RIXS spectrum follows the magnon dispersion [11, 19, 21, 69, 74]. For the cuprates, these results put L edge RIXS as a technique on equal footing with neutron scattering. The first observation of magnetic excitations with RIXS was done by Harada *et al.* [71], who claim to see two-magnon excitations at the oxygen K edge.

We distinguish between magnetic RIXS processes that locally change the size of the magnetic moment and those that do not. The final state contains respectively a longitudinal or a transversal magnetic excitation. Transitions with $\Delta S = 1$ and 2 are allowed for certain magnetic ions, for instance, a transition of

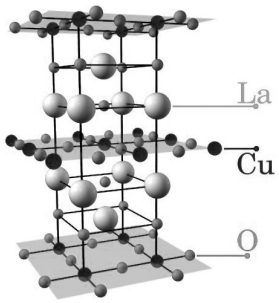


**Figure 4.1:** The crystal structure of $La_2CuO_4$. The $CuO_2$ layers are separated by electronically inactive LaO layers. Figure by M. Berciu.

high spin $Ni^{2+}$ to its low spin state. The energy scale of excitations with $\Delta S \neq 0$ is set by Hund's rule coupling $J_H$, which is typically of the order of 1 eV. These excitations therefore have a much higher energy than the transversal ones, whose energy scale is usually set by the superexchange constant $J \sim 100$ meV. Magnetic excitations with $\Delta S \neq 0$ are described in chapter 3, and are beyond the scope of this chapter.

This chapter starts with a brief review of the theory for magnetic excitations in cuprates in Sec. 4.2. The following sections contain a general formulation of the magnetic RIXS cross section (Sec. 4.3), which is then applied in Sec. 4.4 to the copper K edge, in Sec. 4.5 to the copper L and M edges, and to the oxygen K edge in Sec. 4.7. Finally, the relevance of the screening of a magnetic impurity in the Heisenberg model for angle-resolved photo-emission spectroscopy will be discussed in Sec. 4.8.

## 4.2 Theory of magnetic excitations

### 4.2.1 Electronic structure of cuprates

All work in this chapter is focussed on cuprate superconductors and their Mott insulating parent compounds. The cuprates investigated here have a perovskite structure, as shown in Fig. 4.1 for $La_2CuO_4$: layers of $CuO_2$ are stacked on top of each other, sometimes separated by a different layer (as in $La_2CuO_4$).

The copper ions are often situated at the center of octahedrons of oxygen ions. In the insulating state, the copper 3d subshell contains (approximately) 9 electrons, while the surrounding oxygen ions are in a $2p^6$ configuration, so they have a charge of $-2e$. This creates a crystal field that splits the Cu 3d states. If the oxygen ions form a perfectly cubic octahedron, the 5 Cu 3d levels are split in a $t_{2g}$ triplet and an $e_g$ doublet, see Fig. 4.2. The $e_g$ orbitals point towards the negatively charged oxygen ions, and therefore have a higher Coulomb energy than the $t_{2g}$ orbitals (which are directed away from the oxygen ions). Because of the stacking of the $CuO_2$ layers, the octahedra are usually elongated along the $z$ axis (perpendicular to the $CuO_2$ planes), which splits the $t_{2g}$ and $e_g$ levels

further, as shown in Fig. 4.2. In $La_2CuO_4$, for instance, the hole in the 3d subshell populates the $3d_{x^2-y^2}$ orbital in the ground state: the $3d_{3z^2-r^2}$ orbital is lowered in energy because its Coulomb interaction with the apical oxygen ions (*i.e.*, those along the $z$ axis) is reduced. In other compounds, like $Nd_2CuO_4$ and $CaCuO_2$, the apical oxygens are absent, which could be regarded as if they are moved to infinity. Because the crystal field splitting is of the order of 2 eV in the insulating cuprates [70], the 3d orbital degree of freedom is frozen out already far above room temperature.

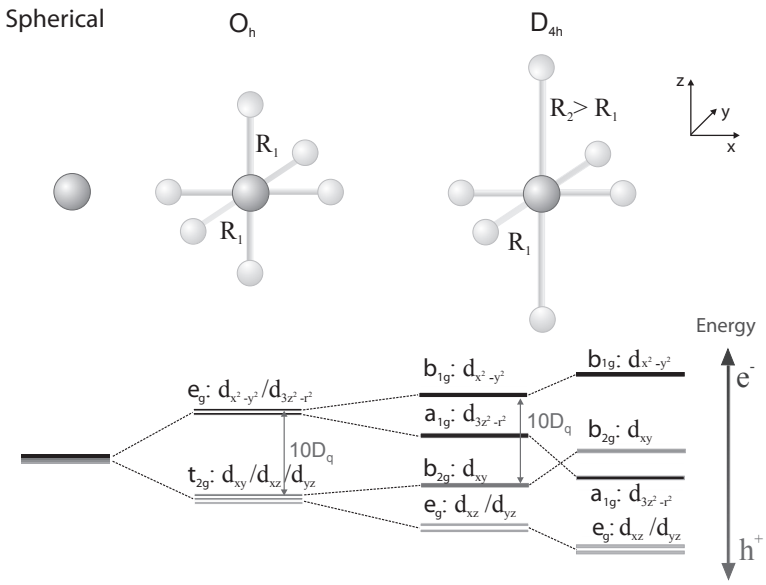


**Figure 4.2:** Crystal field splitting of the Cu 3d levels in an octahedral environment ($O_h$ symmetry) and in an elongated octahedron ($D_{4h}$ symmetry). Figure reproduced with permission from Ref. [70].

The electronic state of a $3d^9$ copper ion is still degenerate however, due to the spin degree of freedom. Superexchange interactions between neighboring Cu ions can split the spin states. In an antiferromagnetic superexchange process, a hole hops to a neighboring Cu ion that is populated by another hole of different spin. The latter hole moves in the opposite direction, and the two holes have effectively exchanged their spin [75]. Because of the Pauli exclusion principle, neighboring holes with the same spin cannot move to each other's site. This confinement increases their kinetic energy, and therefore the superexchange interaction is antiferromagnetic. In case the spins cannot reach each other's places as described above, as for instance when the Cu-O-Cu bonds make 90° angles, weakly ferromagnetic superexchange interactions can arise [76].

The undoped cuprates are well described at low temperature by the $S = 1/2$

Heisenberg model:

$$H_0 = J \sum_{\langle i,j \rangle} \mathbf{S}_i \cdot \mathbf{S}_j, \tag{4.1}$$

where the sum is over all pairs $i, j$ of nearest neighbors.

The direction of the staggered magnetization is not yet fixed by the Heisenberg model; the isotropy is broken by perturbations. In the cuprates, the direction of the staggered magnetization is particularly important for single-magnon RIXS: alignment in the $CuO_2$ planes gives the strongest signal. This alignment is favored by, for instance, the Dzyaloshinsky-Moriya interaction that arises when the $CuO_6$ octahedra are rotated around the [110] direction [77, 78].

### 4.2.2 Boson mappings of the 2D Heisenberg model

No exact solution of the Heisenberg model in 2 dimensions is known. An approximate solution can be obtained by bosonizing the spins [79,80]. There are various boson formulations. We briefly review the Holstein-Primakoff and Dyson-Maleev approaches here.

**Spin to boson mappings.** In both boson mappings, the state of the spin is represented by a single boson mode. The state $|S, m\rangle$ with $m = +S$ is identified with the boson vacuum state. If the spin is lowered by $n$ units, the state $m = S-n$ is represented by $n$ bosons in the mode, etc. The angular momentum identities

$$\langle S, m | \, S^z \, | S, m \rangle = \hbar m \tag{4.2}$$

$$\langle S, m \pm 1 | \, S^\pm \, | S, m \rangle = \hbar \sqrt{S(S+1) - m(m \pm 1)} \tag{4.3}$$

fix $S^z = \hbar(S - a^\dagger a)$, where $a^{(\dagger)}$ creates (annihilates) a boson. The bosons satisfy $[a, a^\dagger] = 1$. The form of the raising and lowering operators $S^\pm$ differs for the two mappings. In the Holstein-Primakoff mapping,

$$S^+ = \hbar\sqrt{2S}\sqrt{1 - \frac{a^\dagger a}{2S}}\; a \quad \text{and} \quad S^- = (S^+)^\dagger. \tag{4.4}$$

It can be easily verified that this mapping satisfies Eq. (4.3). The square-root of the boson operators is defined by the expansion $\sqrt{1-x} = 1 - x/2 - x^2/8 - \ldots$ This boson mapping satisfies the angular momentum commutation relations.

The expansion of the square-root introduces infinitely many multi-boson terms. This complicates the boson mapping as one has to decide where to cut off this expansion in practical calculations. The (conjugate) Dyson-Maleev mapping solves this problem by the alternative definition

$$S^+ = \hbar a, \tag{4.5}$$

$$S^- = \hbar\sqrt{2S} a^\dagger \left(1 - \frac{a^\dagger a}{2S}\right). \tag{4.6}$$

Note that with this mapping, $(S^+)^\dagger \neq S^-$. For convenience, we will set $\hbar = 1$ from hereon.

Both boson formulations suffer from the problem that the Hilbert spaces are not the same before and after the boson mapping: the boson mode can be populated by any number of bosons, which makes the Hilbert space infinite. On the other side, the spin can only be in $2S + 1$ orthogonal states. Boson states with more than $2S$ bosons are therefore unphysical. Although $S^\pm$ do not take one out of the physical Hilbert space, they do if one approximates the square-root in the Holstein-Primakoff formulation. Therefore, all spin operators should be projected on the physical subspace after expansion of the square-root [81].

**Holstein-Primakoff theory for the Heisenberg antiferromagnet.** When boson theories are applied to the Heisenberg antiferromagnet, each spin in the system is represented by a boson mode. One takes the classical, antiferromagnetic Néel state as the reference state: it is identified with the boson vacuum. The boson vacuum should not be confused with the (approximate) ground state; it is just a zeroth order approximation to it, which will be refined within the boson formalism. When defining the Holstein-Primakoff bosons above, we assumed that the $m = S$ state was directed along the $z$ direction. Therefore, we rotate the spin operators for every site to align them with the ordered moment. Then, we can still use the same boson definitions as above. Since the Heisenberg Hamiltonian is invariant under rotations, we might as well take spins of the spin-up sublattice to be aligned along the $z$ axis, so that only the spins of the spin-down sublattice have to be rotated by 180° around the $x$ axis: $S^\pm \mapsto S'^\mp$ and $S^z \mapsto -S'^z$. In these locally rotated coordinates, the antiferromagnetic Heisenberg model is

$$H_0 = J \sum_{i\in\uparrow,\delta} \left( -S'^z_i S'^z_{i+\delta} + \frac{1}{2}\left[ S'^+_i S'^+_{i+\delta} + S'^-_i S'^-_{i+\delta} \right] \right) \tag{4.7}$$

where the sum over $i$ is only over the spin-up sublattice, and $\delta$ points to the nearest neighbors. In terms of Holstein-Primakoff bosons, the Hamiltonian consists of two-boson terms and also many multi-boson interaction terms.

The Hamiltonian can be approximated by neglecting all interaction terms: all square roots are approximated with 1. This so-called linear spin wave theory becomes exact in the limit of large spin, but also turns out to work reasonably well for $S = 1/2$. One obtains

$$H_0 = -\frac{JzNS^2}{2} + JS \sum_{i\in\uparrow,\delta} \left( a^\dagger_i a_i + a^\dagger_{i+\delta} a_{i+\delta} + a_i a_{i+\delta} + a^\dagger_i a^\dagger_{i+\delta} \right), \tag{4.8}$$

where the constant represents the energy of the classical Néel state. A Fourier transform gives

$$H_0 = -\frac{JzNS^2}{2} + \frac{JzS}{2} \sum_{\mathbf{k}} \left( 2a^\dagger_{\mathbf{k}} a_{\mathbf{k}} + \gamma_{\mathbf{k}} \left( a_{-\mathbf{k}} a_{\mathbf{k}} + a^\dagger_{-\mathbf{k}} a^\dagger_{\mathbf{k}} \right) \right), \tag{4.9}$$

where $\gamma_{\mathbf{k}} = \sum_\delta e^{i\mathbf{k}\cdot\boldsymbol{\delta}}/z$ with $z$ the number of nearest neighbors. The result is Bogoliubov transformed as $a_{\mathbf{k}} = u_{\mathbf{k}}\alpha_{\mathbf{k}} - v_{\mathbf{k}}\alpha^\dagger_{-\mathbf{k}}$, where

$$u_{\mathbf{k}} = \sqrt{\frac{1}{2\sqrt{1-\gamma_{\mathbf{k}}^2}} + \frac{1}{2}} \quad \text{and} \quad v_{\mathbf{k}} = \text{sign}(\gamma_{\mathbf{k}})\sqrt{\frac{1}{2\sqrt{1-\gamma_{\mathbf{k}}^2}} - \frac{1}{2}}. \tag{4.10}$$

Since the cuprates studied in this thesis are (approximately) invariant under inversion of space, $\gamma_{\mathbf{k}} = \gamma_{-\mathbf{k}}$, $u_{\mathbf{k}} = u_{-\mathbf{k}}$ and $v_{\mathbf{k}} = v_{-\mathbf{k}}$, and one obtains

$$H_0 = -\frac{JzNS^2}{2} + JzS\sum_{\mathbf{k}}\left(v_{\mathbf{k}}^2 - \gamma_{\mathbf{k}}u_{\mathbf{k}}v_{\mathbf{k}}\right) + \sum_{\mathbf{k}}\omega_{\mathbf{k}}\alpha^\dagger_{\mathbf{k}}\alpha_{\mathbf{k}}. \tag{4.11}$$

The Bogoliubov bosons are called magnons and are the quanta of the spin wave modes. Their dispersion is

$$\omega_{\mathbf{k}} = JzS\sqrt{1-\gamma_{\mathbf{k}}^2}. \tag{4.12}$$

The ground state (the magnon vacuum) has a reduced energy with respect to the Néel state because of quantum fluctuations. The magnon vacuum $|0\rangle$ is defined by $\alpha_{\mathbf{p}}|0\rangle = 0$, and is related to the Néel state $|\text{Néel}\rangle$ by

$$|0\rangle = e^{\sum_{\mathbf{k}}\theta_{\mathbf{k}}\left(a^\dagger_{\mathbf{k}}a^\dagger_{-\mathbf{k}} - a_{\mathbf{k}}a_{-\mathbf{k}}\right)}|\text{Néel}\rangle = e^{\sum_{i,j}\theta_{ij}\left(a_i^\dagger a_j^\dagger - a_j a_i\right)}|\text{Néel}\rangle \tag{4.13}$$

where $\tanh 2\theta_{\mathbf{k}} = -v_{\mathbf{k}}/u_{\mathbf{k}}$. In real space, $\theta_{ij} = \frac{1}{N}\sum_{\mathbf{k}} e^{i\mathbf{k}\cdot(\mathbf{R}_i - \mathbf{R}_j)}\theta_{\mathbf{k}}$. Note that $\theta_{\mathbf{k}}$ and $\theta_{ij}$ are real, so $\theta_{ij} = \theta_{ji}$. Further, $\theta_{\mathbf{k}+(\pi,\pi)} = -\theta_{\mathbf{k}}$, so $\theta_{ii} = 0$. Numerical evaluation shows that $\theta_{ij}$ is of the order of $\pm 0.02$, which means that the magnon vacuum is quite close to the Néel state.

Because of the breaking of rotational invariance of the Heisenberg model by the antiferromagnetic ground state, a Goldstone boson is present. Indeed, the magnon dispersion goes to zero at the $\Gamma$ point. Magnon-magnon interactions do not change the spectrum at the $\Gamma$ point, and magnons around $\mathbf{k} = (0,0) \equiv \mathbf{0}$ are stable against decay into multiple bosons.

The Heisenberg model appears from the more general Hubbard model when correlations are very strong compared to the hopping. Starting from a single band Hubbard model, one can expand in the small parameter $t/U$ and obtain, to lowest order, the Heisenberg model: the charge degree of freedom of the Hubbard model is frozen out, and only the spin degree of freedom remains. The next order contains further-neighbor exchange interactions, including ring exchange, which rearranges 4 neighboring spins on a square plaquette. The latter interaction is relatively strong because there are many hopping processes that lead to such

interactions. The result of the expansion in $t/U$ to fourth order is

$$H_0 = \left(\frac{4t^2}{U} - \frac{24t^4}{U^3}\right) \sum_{\langle i,j\rangle_1} \mathbf{S}_i \cdot \mathbf{S}_j + \frac{4t^4}{U^3} \sum_{\langle i,j\rangle_2} \mathbf{S}_i \cdot \mathbf{S}_j + \frac{4t^4}{U^3} \sum_{\langle i,j\rangle_3} \mathbf{S}_i \cdot \mathbf{S}_j + \frac{80t^4}{U^3} \sum_{\langle i,j,k,l\rangle} [(\mathbf{S}_i \cdot \mathbf{S}_j)(\mathbf{S}_k \cdot \mathbf{S}_l) + (\mathbf{S}_i \cdot \mathbf{S}_l)(\mathbf{S}_j \cdot \mathbf{S}_k) - (\mathbf{S}_i \cdot \mathbf{S}_k)(\mathbf{S}_j \cdot \mathbf{S}_l)] \tag{4.14}$$

where $\langle i,j\rangle_n$ indicates all pairs of $n^{\text{th}}$ neighbors [82]. $\langle i,jk,l\rangle$ indexes all square plaquettes, where $i,j,k,l$ point to the spins on the corners of the squares in clock-wise order. When treated on a mean-field level, the ring exchange term renormalizes the first and second neighbor exchange interactions: $J \mapsto \frac{4t^2}{U} - \frac{64t^4}{U^3}$ and $J' \mapsto -\frac{16t^4}{U^3}$, respectively [83].

The linear spin wave solution of the nearest-neighbor Heisenberg model can be easily extended to interactions between more distant neighbors, as long as the ground state stays antiferromagnetic. The Hamiltonian can be written as

$$H_0 = \frac{1}{2} \sum_{i,j} J_{ij} \mathbf{S}_i \cdot \mathbf{S}_j, \tag{4.15}$$

where $J_{ij}$ is the superexchange coupling between spins $i$ and $j$. The sum is over all $i,j$, and the factor $1/2$ prevents double counting of the bonds. The function $J_{ij}$ is split in two: the first part contains coupling between different sublattices and the second part contains the intra-sublattice couplings. The Fourier transforms of these parts are $J_{\mathbf{k}}$ and $J'_{\mathbf{k}}$ respectively. Again, a Bogoliubov transform can be employed and one finds

$$H_0 = \text{const.} + \sum_{\mathbf{k}} \Omega_{\mathbf{k}} \alpha^\dagger_{\mathbf{k}} \alpha_{\mathbf{k}}, \tag{4.16}$$

where the magnon dispersion is

$$\Omega_{\mathbf{k}} = S\left[(J_{\mathbf{0}} - J'_{\mathbf{0}} + J'_{\mathbf{k}})(U^2_{\mathbf{k}} + V^2_{\mathbf{k}}) - 2J_{\mathbf{k}} U_{\mathbf{k}} V_{\mathbf{k}}\right], \tag{4.17}$$

and the new Bogoliubov coefficients are

$$U_{\mathbf{k}} = \sqrt{\frac{J_{\mathbf{0}} - J'_{\mathbf{0}} + J'_{\mathbf{k}}}{2\sqrt{(J_{\mathbf{0}} - J'_{\mathbf{0}} + J'_{\mathbf{k}})^2 - J^2_{\mathbf{k}}}} + \frac{1}{2}} \quad \text{and} \quad V_{\mathbf{k}} = \text{sign}(J_{\mathbf{k}})(U^2_{\mathbf{k}} - 1). \tag{4.18}$$

## 4.3 Magnetic RIXS scattering amplitude

As explained in Sec. 4.1, both direct and indirect RIXS can probe magnetic excitations, be it of different kind. For direct RIXS, single spin flip excitations

can be made at the $2p, 3p \rightarrow 3d$ edges of transition metal ions because of the large spin-orbit coupling of the $2p$ core hole [19,72,73]. For copper, with its simple $3d^{10}$ intermediate state of the valence electrons, these edges split into intermediate states with total angular momentum in the core states of $J = 1/2$ ($L_2$, $M_2$ edges) and $J = 3/2$ ($L_3$, $M_3$ edges). The edges are well resolved in XAS spectra (particularly at the L edge [84]), and therefore in RIXS one selects either the intermediate states with $J = 1/2$ or $J = 3/2$. This allows neglecting contributions from one edge if the incoming X-ray photons are at resonance with the other, as can be seen explicitly from Eq. (2.41). This is the fast collision approximation. Because the p-like core states have a strong spin-orbit coupling, the spin and orbital angular momentum separately are no longer good quantum numbers in the separated $J = 1/2$ and $3/2$ intermediate states. Therefore orbital and spin orbital angular momentum can be exchanged and direct spin flip processes can in principle be allowed in RIXS, unlike in optical spectroscopy. Because of the superexchange interaction present in the cuprates, single spin flips will disperse: they are in essence a superposition of single magnon states. Direct RIXS is thus able to probe the single magnon dispersion [19, 74].

In addition to spin flip processes, RIXS can also reach final states with a different orbital occupation of the 3d levels via similar scattering channels. These excitations are called dd excitations, and can be accompanied by a spin flip. In Sec. 4.5.1, the cross sections for dd excitations and single spin flip excitations in the cuprates are calculated in a single ion model.

Indirect RIXS is always present, but in general becomes dominant only when direct RIXS is absent. This happens at the K edges of copper and oxygen, because there is no spin-orbit coupling in the 1s levels ($L = 0$). When indirect RIXS is not dominant, one can sometimes use the polarization dependence to resolve the indirect RIXS channel.

In the following, we discuss the polarization dependence (Sec. 4.3.1) of both direct and indirect magnetic RIXS. In Sec. 4.3.2 the mechanisms are discussed by which magnetic excitations are created.

### 4.3.1 Polarization dependence

Since all of the work in this chapter is focused on the cuprates, we analyze here the full RIXS scattering amplitude (2.41) for the Cu K edge and Cu L and M edges. The O K edge is a special case and will be treated separately in Sec. 4.7.

We classify the RIXS processes by the indices $\mu, \nu, \nu'$ and $\mu'$ as in Eq. (2.42), *i.e.*, by the dipole transitions. At the Cu K edge, one excites an electron with spin up or down from the 1s orbital into a 4p orbital: $\mu = 1\mathrm{s}$, $\nu = 4\mathrm{p}_{x,y,z}$. We assume that the 4p electron is a spectator, *i.e.*, it does not interact with the valence electrons [4, 5]. In that case, $\nu' = \nu$, and $\mu' = \mu$. Since the spin of the photo-excited electron is irrelevant if the 4p electron is only a spectator, we can integrate it out without effort. The only remaining index is $\nu\ (= \nu') \in \{4\mathrm{p}_{x,y,z}\}$. Next, one has to determine the energy of the 4p states. Since these are assumed

to be decoupled from the valence electrons, this is a relatively simple task. As explained in Sec. 3.4, band effects play a role, as well as the crystal field. The simplest polarization dependence arises when we assume that all 4p states have an equal energy: the scattering amplitude at the Cu K edge then simplifies to

$$\mathcal{F}_{fg} = T_K(\boldsymbol{\epsilon}', \boldsymbol{\epsilon}) \sum_i e^{i\mathbf{q}\cdot\mathbf{R}_i} \sum_n \frac{\langle f| c^\dagger_{i,1s} |n\rangle \langle n| c_{i,1s} |g\rangle}{E_g + \hbar\omega_{\mathbf{k}} - E_n + i\Gamma}, \tag{4.19}$$

where the 4p states are integrated out, and

$$T_K(\boldsymbol{\epsilon}', \boldsymbol{\epsilon}) = \sum_i \langle 1s| \boldsymbol{\epsilon}'^* \cdot \mathbf{r} |4p_i\rangle \langle 4p_i| \boldsymbol{\epsilon} \cdot \mathbf{r} |1s\rangle \propto \boldsymbol{\epsilon}'^* \cdot \boldsymbol{\epsilon}. \tag{4.20}$$

At the Cu $L_{2,3}$ edges of the cuprates, the indices $\mu$ and $\mu'$ relate to the core orbitals. Since in the intermediate state a $3d^{10}$ configuration is created, the core orbitals do not interact with the on-site valence electrons. If one neglects longer range interactions, the core states decouple from the valence states, and they can be integrated out from the scattering amplitude. To do so, we first find the core hole's eigenstates, which are determined mainly by the core level spin-orbit coupling. They split in two sets ($J = 1/2$ and $J = 3/2$, corresponding to $L_2$ and $L_3$, respectively) which are well-separated in energy: $\sim 20$ eV [84]. Since the separation is an order of magnitude larger than $\Gamma$, we neglect any contribution from one edge ($L_2$ or $L_3$) if the X-ray photons are tuned to the other. At the $L_2$ edge, we therefore sum over the $J = 1/2$ core states $\mu = \mu'$ with $m_J = \pm 1/2$:

$$|m_J = +1/2\rangle = \sqrt{\tfrac{1}{3}} \left(|p_z \uparrow\rangle + |p_x \downarrow\rangle + i\,|p_y \downarrow\rangle\right), \tag{4.21}$$

$$|m_J = -1/2\rangle = \sqrt{\tfrac{1}{3}} \left(|p_z \downarrow\rangle - |p_x \uparrow\rangle + i\,|p_y \uparrow\rangle\right) \tag{4.22}$$

At the $L_3$ edge, we sum over all $J = 3/2$ core states

$$|m_J = +3/2\rangle = -\sqrt{\tfrac{1}{2}} \left(|p_x \uparrow\rangle + i\,|p_y \uparrow\rangle\right), \tag{4.23}$$

$$|m_J = +1/2\rangle = \sqrt{\tfrac{2}{3}}\,|p_z \downarrow\rangle + \sqrt{\tfrac{1}{6}} \left(|p_x \downarrow\rangle + i\,|p_y \downarrow\rangle\right), \tag{4.24}$$

$$|m_J = -1/2\rangle = \sqrt{\tfrac{2}{3}}\,|p_z \downarrow\rangle + \sqrt{\tfrac{1}{6}} \left(|p_x \uparrow\rangle - i\,|p_y \uparrow\rangle\right), \tag{4.25}$$

$$|m_J = -3/2\rangle = \sqrt{\tfrac{1}{2}} \left(|p_x \downarrow\rangle - i\,|p_y \downarrow\rangle\right). \tag{4.26}$$

When the core hole degree of freedom is integrated out from the scattering amplitude, we find for the $L_{2/3}$ edge:

$$\mathcal{F}_{fg} = \sum_{\nu'} T_{L_{2/3},\nu'}(\boldsymbol{\epsilon}', \boldsymbol{\epsilon}) \sum_i e^{i\mathbf{q}\cdot\mathbf{R}_i} \sum_n \frac{\langle f| c_{i,\nu'} |n\rangle \langle n| c^\dagger_{i,\nu} |g\rangle}{E_g + \hbar\omega_{\mathbf{k}} - E_n + i\Gamma}, \tag{4.27}$$

where the spin-orbital $\nu$ is fixed by the initial state: $c^\dagger_\nu$ fills the 3d hole of the initial state. $\nu'$ labels the different scattering channels. For example, $\nu' = \nu$ is the elastic scattering channel, and when $\nu'$ describes an electron in the same orbital as $\nu$, but with opposite spin, we have spin flip scattering. Also, dd excitations can be described when $\nu'$ refers to other 3d orbitals than $x^2$-$y^2$.

Note that the Cu L and M edges are very similar: only the radial wave functions of the core states differ, giving different overal intensities; the angular parts are the same. The main difference between the edges is the maximum $\mathbf{q}$, which is larger at the L edge.

### 4.3.2 Direct & indirect magnetic RIXS – UCL expansion

After splitting off the polarization dependence from the scattering amplitude, the next step in obtaining the (approximate) cross sections of magnetic RIXS on the antiferromagnetic cuprates is to deal with the intermediate states. The UCL expansion (see Sec. 2.5) offers a convenient way to do that, as the energy scale of the magnetic excitations is usually much lower than $\Gamma$. To zeroth order, the Kramers-Heisenberg amplitude (2.41) is reduced to the operation of two dipole operators; there is not enough time available to allow for dynamics in the intermediate state. This is equivalent to the fast collision approximation [26], which is a good approximation to the direct RIXS scattering amplitude of 2D cuprates [11, 19, 21, 74].

At the Cu K edge, the direct scattering channel does not give inelastic intensity, but at the Cu $L_{2,3}$ and $M_{2,3}$ edges, spin flip processes can occur to zeroth order in the UCL expansion, as explained in Sec. 4.3.1. We get for the zeroth order

$$\mathcal{F}^{(0)}_{fg} = \frac{T_{\mathrm{sf}}(\boldsymbol{\epsilon}', \boldsymbol{\epsilon})}{i\Gamma} \langle f| \sum_i e^{i\mathbf{q}\cdot\mathbf{R}_i} c_{i\bar{\sigma}} c^\dagger_{i\sigma} |g\rangle \,, \tag{4.28}$$

where $T_{\mathrm{sf}}$ is the polarization factor for spin flip processes, and $\sigma$ is the spin of the 3d hole (assuming it is fully polarized). $\bar{\sigma}$ is the opposite spin of $\sigma$. This amplitude will be discussed in more detail in Sec. 4.5.1.

To get the leading order scattering amplitude for the Cu K edge, we proceed to the next order of the UCL expansion, which introduces intermediate state dynamics:

$$\mathcal{F}^{(1)}_{fg} = \frac{T_K(\boldsymbol{\epsilon}', \boldsymbol{\epsilon})}{i\Gamma} \langle f| \sum_i e^{i\mathbf{q}\cdot\mathbf{R}_i} c^\dagger_{i,1s} \frac{\bar{H}}{i\Gamma} c_{i,1s} |g\rangle \,. \tag{4.29}$$

The 4p electrons have been integrated out since they are assumed to be spectators. The Hamiltonian describes the dynamics around the core hole site, where the superexchange bonds are frustrated. This creates two-magnon excitations, as will be discussed in Sec. 4.4. Higher orders of the UCL expansion will add excitations with even numbers of magnons. Odd numbers of magnons are not allowed because the Heisenberg form of the magnetic bonds conserves the total spin. A single magnon carries spin 1.

A simple example is given by the Heisenberg ferromagnet. At the Cu $L_{2,3}$ edges, the spin flip channel allows for single magnon scattering. The inelastic weight at the Cu K edge is zero because $\bar{H}$ rearranges the spins of a ferromagnet, which cannot create two-magnon excitations.

It might not be obvious from Eq. (4.28) that RIXS can measure the dispersion of magnons: the spin is flipped on site $i$, while the magnon is a highly delocalized magnetic excitation. One should keep in mind, however, that the incident photon can be scattered at any equivalent site, leading to a final state that is a superposition of spin flips at equivalent sites. Such a final state carries a non-local magnetic excitation with momentum $\hbar\mathbf{q}$. Just as in neutron scattering, the RIXS cross section therefore consists of a local structure factor (2.42) depending on the polarization and the excitation mechanism, multiplied by the appropriate spin susceptibility [19, 74]. For non-interacting spins, the susceptibility is uniform and featureless, but for systems with interatomic spin-spin interactions the susceptibility acquires a strong $\mathbf{q}$ dependence, which may be measured in momentum-resolved RIXS.

## 4.4 Copper K edge

Published as '*Magnetic Excitations in $La_2CuO_4$ probed by Indirect Resonant Inelastic X-ray Scattering*' in Phys. Rev. B **77**, 134428 (2008) with Fiona Forte and Jeroen van den Brink.

**Abstract.** Recent experiments on $La_2CuO_4$ suggest that indirect resonant inelastic X-ray scattering (RIXS) might provide a probe for transversal spin dynamics. We present in detail a systematic expansion of the relevant magnetic RIXS cross section by using the ultrashort core hole lifetime (UCL) approximation. We compute the scattering intensity and its momentum dependence in leading order of the UCL expansion. The scattering is due to two-magnon processes and is calculated within a linear spin wave expansion of the Heisenberg spin model for this compound, including longer range and cyclic spin interactions. We observe that the latter terms in the Hamiltonian enhance the first moment of the spectrum if they strengthen the antiferromagnetic ordering. The theoretical spectra agree very well with experimental data, including the observation that scattering intensity vanishes for the transferred momenta $\mathbf{q} = (0, 0)$ and $\mathbf{q} = (\pi, \pi)$. We show that at finite temperature there is an additional single-magnon contribution to the scattering with a spectral weight proportional to $T^3$. We also compute the leading corrections to the UCL approximation and find them to be small, putting the UCL results on a solid basis. All this univocally points to the conclusion that the observed low temperature RIXS intensity in $La_2CuO_4$ is due to two-magnon scattering.

**Introduction.** In indirect RIXS, the energy of the incoming photons is tuned to match a resonance that corresponds to exciting a core electron to an outer shell. The K edge of transition metal ions is particularly useful since it promotes a 1s core electron to an outer 4p shell, which is well above the Fermi level, so that the X-rays do not cause direct transitions of the 1s electron into the lowest 3d-like conduction bands [2, 44, 46, 57, 85–95].

Due to the large energy involved ($\sim 5-10$ keV), the core hole is ultrashortlived and it induces an almost delta function-like potential (in time) on the valence electrons [48–50]. Consequently, elementary excitations of the valence electrons will screen the local potential, but have little time to do so. When the core hole decays, the system can be left behind in an excited state. By observing the energy and momentum of the outgoing photon, one probes the elementary excitations of the valence electrons including, in particular, their momentum dependence.

Recently, RIXS measurements performed by J.P. Hill *et al.* on the high-$T_c$ cuprate superconductor $La_{2-x}Sr_xCuO_4$ revealed that RIXS is potentially able to detect *transversal* spin excitations – magnons [14]. Later, Ellis *et al.* confirmed these measurements in a follow-up experiment [53]. The experiments show that the magnetic RIXS signal is strongest in the undoped cuprate $La_2CuO_4$. The magnetic loss features are at energies well below the charge gap of this magnetic insulator, at energies where the charge response function $S(\mathbf{q}, \omega)$ vanishes (see chapter 3), as well as the *longitudinal* spin one – which is in fact a higher order charge response function. The proposed scattering mechanism is a two-magnon scattering process in which two spin waves are created [14, 51].

In a previous theoretical analysis it was shown that the magnetic correlation function that is measured by indirect RIXS is a four-spin correlation one, probing two-magnon excitations [51]. This makes indirect RIXS a technique that is essentially complementary to magnetic neutron scattering, which probes single magnon properties and two-spin correlations. In this section, we present the theoretical framework of Ref. [51] in more detail and use it for an analysis of the experimental magnetic RIXS data on perovskite $CuO_2$ layers of $La_2CuO_4$.

We expand upon the previous considerations by providing a detailed comparison between the theory and experiment, including also longer range magnetic exchange interactions in the theory, with values known from neutron scattering data. We develop the theory to account also for the effects of finite temperature, which give rise to a non-trivial single-magnon contribution to the RIXS signal. We also compare with the results of Nagao and Igarashi [96], who computed the magnetic RIXS spectra based on the theoretical framework of Ref. [51], taking also some of the magnon-magnon interactions into account.

The theory is developed on basis of the UCL expansion. We compute leading order corrections to this expansion and show that they are small. This makes sure that the UCL approximation provides a reliable route to analyze the indirect RIXS spectra.

This section is organized as follows: first we obtain an expression for the cross section of the 2D $S = 1/2$ Heisenberg antiferromagnet in linear spin wave theory

in terms of magnon creation and annihilation operators. Then we evaluate the cross section at $T = 0$ and we also consider the low temperature case. Next, the leading correction to the cross section in the UCL approximation is calculated. Finally, we will present our conclusions.

**Cross Section for Indirect RIXS on a Heisenberg AFM.** Recently, Hill *et al.* [14] and Ellis *et al.* [53] observed that RIXS on the high-$T_c$ superconductor $La_{2-x}Sr_xCuO_4$ picks up transversal spin dynamics: magnons. In the undoped regime, the RIXS intensity turns out to be highest. The same feature was observed in the related compound $Nd_2CuO_4$ [14]. These cuprates consist of perovskite $CuO_2$ layers with a hole in the Cu 3d subshell. The low energy spin dynamics of these systems are properly described by a single band Hubbard model at half filling. The strong interactions between holes in the Cu 3d subshells drive these materials into the Mott insulating regime, where the low energy excitations are the ones of the $S = 1/2$ 2D Heisenberg antiferromagnet (4.1) with $J \approx 146$ meV for nearest neighbors [83]. In the antiferromagnetic groundstate, the Hamiltonian can be bosonized in linear spin wave theory (LSWT) where $S_i^z \mapsto 1/2 - a_i^\dagger a_i$, $S_i^+ \mapsto a_i$ and $S_i^- \mapsto a_i^\dagger$ for $i \in A$ ($A$ being the sublattice with spin-up) and $S_j^z \mapsto b_j^\dagger b_j - 1/2$, $S_j^+ \mapsto b_j^\dagger$ and $S_j^- \mapsto b_j$ for $j \in B$ (the spin-down sublattice). Note that we now introduce two boson species in a doubled unit cell, so the Brillouin zone will be twice as small as before in Sec. 4.2. A Bogoliubov transformation in reciprocal space is necessary to diagonalize the Heisenberg Hamiltonian:

$$\alpha_{\mathbf{k}} = U_{\mathbf{k}} a_{\mathbf{k}} + V_{\mathbf{k}} b_{-\mathbf{k}}^\dagger, \tag{4.30}$$

$$\beta_{\mathbf{k}} = U_{\mathbf{k}} b_{\mathbf{k}} + V_{\mathbf{k}} a_{-\mathbf{k}}^\dagger \tag{4.31}$$

with $U_{\mathbf{k}}$, $V_{\mathbf{k}}$ as in Eq. (4.18). For interactions up to third nearest neighbors we get

$$J_{\mathbf{k}} = J\left(\cos ak_x + \cos ak_y\right) \tag{4.32}$$

$$J'_{\mathbf{k}} = 2J' \cos ak_x \cos ak_y + J''\left(\cos 2ak_x + \cos 2ak_y\right) \tag{4.33}$$

with $a$ the lattice constant and $J, J', J''$ the first through third nearest neighbor couplings. The final linear spin wave Hamiltonian in terms of boson operators is

$$H_0 = \text{const} + \sum_{\mathbf{k}} \Omega_{\mathbf{k}} \left(\alpha_{\mathbf{k}}^\dagger \alpha_{\mathbf{k}} + \beta_{\mathbf{k}}^\dagger \beta_{\mathbf{k}}\right) \tag{4.34}$$

with $\Omega_{\mathbf{k}}$ as in Sec. 4.2.

Our aim is to understand how this picture changes when doing indirect RIXS. In RIXS, one uses X-rays to promote a Cu 1s electron to a 4p state. For an ultrashort time, one creates a core hole at a certain site which lowers the Coulomb repulsion $U$ on that site with an amount $U_c$. As in chapter 3, we again assume

that the core hole potential is local; *i.e.*, it acts only at the core hole site. This approximation is reasonable as the Coulomb potential is certainly largest on the atom where the core hole is located. Moreover, we can consider the potential generated by both the localized core hole and photo-excited electron at the same time. As this exciton is a neutral object, its monopole contribution to the potential vanishes for distances larger than the exciton radius. The multi-polar contributions that we are left with in this case are generally small and drop off quickly with distance.

The strong core hole potential in the intermediate state alters the superexchange processes between the 3d valence electrons. This causes RIXS to couple to multi-magnon excitations, as was first pointed out in Ref. [51]. The simplest microscopic mechanism for this coupling is obtained within the strong-coupling Hubbard model, in which the doubly occupied and empty virtual states shift in energy in presence of the core hole [51, 96]. Adding the amplitudes for the two possible processes shown in Fig. 4.3 leads to an exchange integral in presence of a core hole on site $i$ of

$$J_{ij}^{c} = \frac{2t_{ij}^{2}}{U + U_c} + \frac{2t_{ij}^{2}}{U - U_c} = J_{ij}\,(1 + \eta) \tag{4.35}$$

where $j$ is a site neighboring to $i$ and $\eta = U_c^2/(U^2 - U_c^2)$. This enables us to write down the generic Hamiltonian for the intermediate states [51]:

$$H_{\text{int}} = H_0 + \eta \sum_{i,j} s_i\, s_i^{\dagger} J_{ij} \mathbf{S}_i \cdot \mathbf{S}_j \tag{4.36}$$

where $s_i$ creates a core hole and $s_i^{\dagger}$ annihilates one at site $i$. In the Hubbard framework, one could identify $U$ with the Coulomb energy associated with two holes in a 3d orbital, $U_d = 8.8$ eV, which together with $U_c = 7.0$ eV [97, 98] leads to $\eta = 1.7$; from $U/U_c = 2/3$, as suggested in Ref. [99], one finds $\eta = -0.8$.

The situation in the cuprates, however, is more complex and one needs to go beyond the single band Hubbard model to obtain a value of $\eta$ from microscopic considerations. We will do so by considering a three-band model in the strong coupling limit. However, it should be emphasized that for the end result – the computed RIXS spectrum in the UCL approach – $\eta$ just determines the overall scale of the inelastic scattering intensity. As we will show, higher order corrections in the UCL approach are determined by the value of $\eta$, because $\eta J/\Gamma$ appears as a small parameter in this expansion. As for the cuprates $J/\Gamma \approx 1/5$, such corrections are small for the relevant possible values of $\eta$.

In the three-band Hubbard model that includes also the oxygen states, two important kinds of intermediate states appear: the poorly- and well-screened ones. Because the Coulomb interaction of the core-hole with the valence electrons is large ($U_c = 7.0$ eV, compared to a charge transfer energy $\Delta = 3.0$ eV [98]), a copper hole can transfer to a neighboring oxygen to form a well-screened intermediate state. The low-energy sector now also encompasses an oxygen hole,

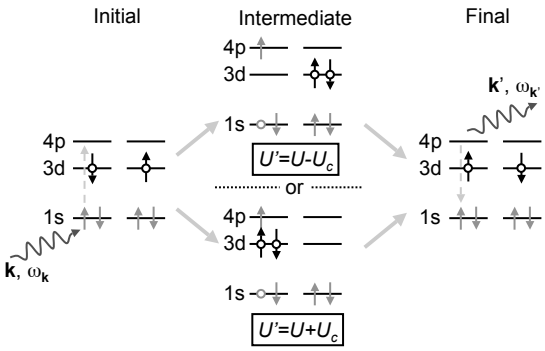


**Figure 4.3:** In RIXS, a photon tuned to the K edge of a transition metal ion creates a core hole at a certain site. The superexchange interaction between this site and a neighboring site is modified because the energy of the virtual intermediate states is changed. The same-site Coulomb repulsion $U$ is lowered by $U_c$ if the core hole site contains no holes and is raised by $U_c$ if there are two holes present. Summing the amplitudes for both processes, we obtain the modified superexchange interaction [see Eq. (4.35)].

equally distributed over the ligands. We will show that, starting from a three band Hubbard model, Eq. (4.36) gives a proper description of both the well- and poorly-screened intermediate states, with $\eta$ now a function of the parameters of the three band model. Before presenting these results we remark that scattering processes that scatter a well-screened state into a poorly-screened state or vice versa yield a large energy loss $\hbar\omega$. These are not important at low $\omega$, where one will only observe scattering in the magnetic channel, not the charge one.

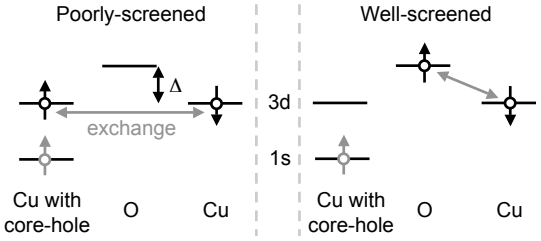


**Figure 4.4:** Modification of the superexchange interaction in the well- and poorly-screened intermediate states. In the poorly-screened state, the core hole potential $U_c$ modifies the superexchange. For the well-screened state, however, the copper 3d hole on the core hole site is transfered to a neighboring oxygen ion, and superexchange is only of order $\mathcal{O}(t_{pd}^2)$, independent of $U_c$.

The magnetic scattering processes for the poorly-screened state are very similar to the single band picture: all copper ions have one hole and all oxygen ions are filled-shell. The superexchange processes are shown in Fig. (4.4). We consider the Anderson and Geertsma contributions to the superexchange [97] and find

$$\eta_{ps} = \frac{U_d\Delta^2(U_p+2\Delta)}{2(2U_d+2\Delta+U_p)}\left(\frac{1}{(U_d-U_c)(U_c-\Delta)^2}+\frac{1}{(U_d+U_c)\Delta^2} + \frac{\left[1/\Delta+1/(\Delta-U_c)\right]^2}{2\Delta-U_c+U_p}\right)-1, \tag{4.37}$$

which results in $\eta = -0.3$ using the parameters $U_d = 8.8$ eV, $U_p = 6.0$ eV, $t_{pd} = 1.3$ eV, $\Delta = 3.0$ eV, and $U_c = 7.0$ eV [97, 98], where $t_{pd}$ is the copper-oxygen hoping integral and $U_p$ the on-site Coulomb repulsion of two oxygen holes.

The well-screened intermediate states have a similarly modified superexchange interaction, as shown in Fig. 4.4. Because of the large core hole Coulomb interaction, an electron from the neighboring oxygen atoms moves in to screen it, or, equivalently, the copper hole is transferred to the in-plane oxygen ions. Transfer out of the plane is not considered since the Cu $3d_{x^2-y^2}$ hole only couples to the in-plane oxygens. Because the Cu hole is transfered in the direction of one of its neighboring Cu ions, the contribution to the superexchange interaction for the well-screened state is of second order in $t_{pd}$, instead of fourth order between two Cu sites (see Fig. 4.4). The rotational invariance around the core-hole site of the transfered hole ensures that the intermediate state Hamiltonian of the form Eq. (4.36) gives the correct scattering amplitude. To lowest order in $t_{pd}$ we hence find

$$\eta_{ws} = \frac{U_d(U_d+U_p)\Delta^2(U_p+2\Delta)}{2(U_d-\Delta)t_{pd}^2(2U_d+U_p+2\Delta)(U_p+\Delta)}-4, \tag{4.38}$$

which results in $\eta = -1.3$ – again restricting ourselves to superexchange of the Anderson and Geertsma type. We see that to lowest order, the core hole potential $U_c$ does not appear in the well-screened intermediate state. From these microscopic considerations, we conclude that the intermediate state Hamiltonian Eq. (4.36) is the correct one and higher order corrections to it are small because for the cuprates $\eta$ is a number of order unity.

In chapter 3, we have shown in detail how to derive the cross section for RIXS processes with a local core hole using the UCL expansion Eq. (2.49). As in chapter 3, we take the energy $E_i$ of the initial state as a reference energy: $E_i = 0$. We also measure the energy $E_n$ of the intermediate state with respect to the resonance energy $\hbar\omega_{\rm res}$ as before. The detuning of the incoming photon energy from $\hbar\omega_{\rm res}$ is defined as $\hbar\omega_{\rm in} = \hbar\omega_{\mathbf{k}} - \hbar\omega_{\rm res}$. If $\Gamma > E_n$, we can expand the amplitude $\mathcal{F}_{fi}$ in a powerseries (2.49). We assume that the energy of the incoming photon is tuned to the resonance ($\omega_{\rm in} = 0$):

$$\mathcal{F}_{fi} = \frac{1}{i\Gamma}\sum_{l=1}^{\infty}\frac{1}{(i\Gamma)^l}\left\langle f\right|\mathcal{D}^\dagger(H_{\rm int})^l\mathcal{D}\left|i\right\rangle. \tag{4.39}$$

Note that we left out the $l = 0$ term because it only contributes to elastic scattering. The leading order non-vanishing term in the sum is $l = 1$, since the core hole broadening is quite large compared to $J$. At the copper K edge, $2\Gamma \approx 1.5$ eV according to Refs. [100, 101], and $2\Gamma \approx 3$ eV for the closely related ions Mn and Ge according to Refs. [102, 103], which in either case is large compared to $J$. As in the three-band model $\eta = -1.3$ or $-0.3$ for the well- or poorly-screened intermediate state respectively, the largest value we find is $\eta J/\Gamma \approx -0.22$. Note that the UCL expansion therefore converges very well – even faster for the poorly-screened state than for the well-screened state (where $|\eta|$ is larger). It is possible to directly include a number of terms with $l \geq 2$ in the cross section by using the expansion

$$\sum_{l=1}^{\infty} \frac{(H_{\text{int}})^l}{(i\Gamma)^l} \approx \sum_{l=1}^{\infty} \left( \frac{H_0^l}{(i\Gamma)^l} + \frac{H_0^{l-1} H'}{(i\Gamma)^l} \right) + \mathcal{O}\left( [\eta J/\Gamma]^2 \right) \tag{4.40}$$

with $H' = \eta \sum_{i,j} s_i s_i^\dagger J_{ij} \mathbf{S}_i \cdot \mathbf{S}_j$. Since $[H_0, \mathcal{D}] = 0$ and $H_0 |i\rangle \equiv 0$, all terms with $H_0$ on the right can be safely neglected. Using Eq. (4.40), $\mathcal{F}_{fi}$ simplifies to

$$\mathcal{F}_{fi} = \frac{1}{i\Gamma} \frac{\eta}{i\Gamma - \hbar\omega} \langle f | \hat{O}_{\mathbf{q}} | i \rangle \tag{4.41}$$

with the scattering operator

$$\hat{O}_{\mathbf{q}} = \sum_{i,j} e^{i\mathbf{q}\cdot\mathbf{R}_i} J_{ij} \mathbf{S}_i \cdot \mathbf{S}_j, \tag{4.42}$$

where we neglected the polarization dependence in the same way as in Eq. (3.7). The polarization dependence is discussed in more detail in Sec. 3.4.

From Eq. 4.42, we can deduce two important features. First, indirect RIXS probes a momentum dependent four-spin correlation function [51]. Second, $\hat{O}_{\mathbf{q}}$ commutes with the $z$ component of total spin $S^z$, so the allowed scattering processes should leave $S^z$ unchanged. Only an even number of magnons can be created or annihilated.

To bosonize Eq. (4.42), we split $\hat{O}_{\mathbf{q}}$ in four parts,

$$\hat{O}_{\mathbf{q}} = \sum_{i,j \in A} \cdots + \sum_{i,j \in B} \cdots + \sum_{i \in A,\, j \in B} \cdots + \sum_{i \in B,\, j \in A} \ldots \tag{4.43}$$

Next, we rewrite this expression using LSWT as introduced above. Fourier transforming the result gives

$$\begin{aligned} \hat{O}_{\mathbf{q}} = \text{const.} + S \sum_{\mathbf{k}} \Big[ & \left( J'_{\mathbf{k}+\mathbf{q}/2} + J'_{\mathbf{k}-\mathbf{q}/2} - J'_{\mathbf{0}} - J'_{\mathbf{q}} + J_{\mathbf{0}} + J_{\mathbf{q}} \right) \times \\ & \left( a^\dagger_{\mathbf{k}+\mathbf{q}/2} a_{\mathbf{k}-\mathbf{q}/2} + b^\dagger_{\mathbf{k}+\mathbf{q}/2} b_{\mathbf{k}-\mathbf{q}/2} \right) + \\ & \left( J_{\mathbf{k}+\mathbf{q}/2} + J_{\mathbf{k}-\mathbf{q}/2} \right) \left( a_{\mathbf{k}-\mathbf{q}/2} b_{-\mathbf{k}-\mathbf{q}/2} + a^\dagger_{\mathbf{k}+\mathbf{q}/2} b^\dagger_{-\mathbf{k}+\mathbf{q}/2} \right) \Big], \end{aligned} \tag{4.44}$$

and we can write $\hat{O}_{\mathbf{q}}$ in terms of the magnon operators using the inverses of Eqs. (4.30) and (4.31). This leads to

$$\hat{O}_{\mathbf{q}} = \hat{O}^{(1)}_{\mathbf{q}} + \hat{O}^{(2)}_{\mathbf{q}} \tag{4.45}$$

where $\hat{O}^{(1,2)}_{\mathbf{q}}$ are lengthy expressions that contain the one- and two-magnon scattering part respectively. The next section deals with the two-magnon part $\hat{O}^{(2)}_{\mathbf{q}}$ where two magnons are created or annihilated. The one-magnon part $\hat{O}^{(1)}_{\mathbf{q}}$ (where the change in the number of magnons is zero) is treated in Sec. 4.4.

**Two-Magnon Scattering at $T = 0$ K.** At $T = 0$ K, the system is in its ground state, where no magnons are present: $|i\rangle = |0\rangle$. Adding conservation of $S^z$, the only allowed scattering processes are the ones in which two magnons are created, so we consider the two-magnon part of the scattering operator of Eq. (4.45) with $S = 1/2$:

$$\begin{aligned}\hat{O}^{(2)}_{\mathbf{q}} = \sum_{\mathbf{k}\in\mathrm{MBZ}} \Big[ &- \Big( J'_{\mathbf{k}+\mathbf{q}/2} + J'_{\mathbf{k}-\mathbf{q}/2} - J'_{\mathbf{0}} - J'_{\mathbf{q}} + J_{\mathbf{0}} + J_{\mathbf{q}} \Big) \times \\ &\Big( U_{\mathbf{k}+\mathbf{q}/2} V_{\mathbf{k}-\mathbf{q}/2} + U_{\mathbf{k}-\mathbf{q}/2} V_{\mathbf{k}+\mathbf{q}/2} \Big) \\ &+ \Big( J_{\mathbf{k}+\mathbf{q}/2} + J_{\mathbf{k}-\mathbf{q}/2} \Big) \Big( U_{\mathbf{k}+\mathbf{q}/2} U_{\mathbf{k}-\mathbf{q}/2} + V_{\mathbf{k}+\mathbf{q}/2} V_{\mathbf{k}-\mathbf{q}/2} \Big) \Big] \times \\ &\Big( \alpha_{\mathbf{k}-\mathbf{q}/2} \beta_{-\mathbf{k}-\mathbf{q}/2} + \alpha^\dagger_{\mathbf{k}+\mathbf{q}/2} \beta^\dagger_{-\mathbf{k}+\mathbf{q}/2} \Big)\end{aligned} \tag{4.46}$$

The two-magnon spectrum is shown in Fig. 4.5(a). Several remarkable features can be seen.

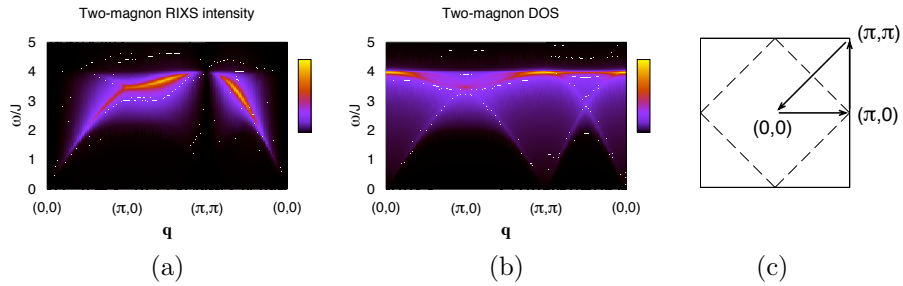


(a) (b) (c)

**Figure 4.5:** RIXS spectrum (a) and two-magnon DOS (b) for a nearest neighbor Heisenberg antiferromagnet with exchange interaction $J$ as a function of transferred momentum $\mathbf{q}$ for a cut through the Brillouin zone (c). The dashed line indicates the magnetic BZ boundary.

First of all the spectral weight vanishes at $\mathbf{q} = (0, 0)$ and $\mathbf{q} = (\pi, \pi)$, as can be seen in Fig. 4.6(b). This is in agreement with experimental observations [14].

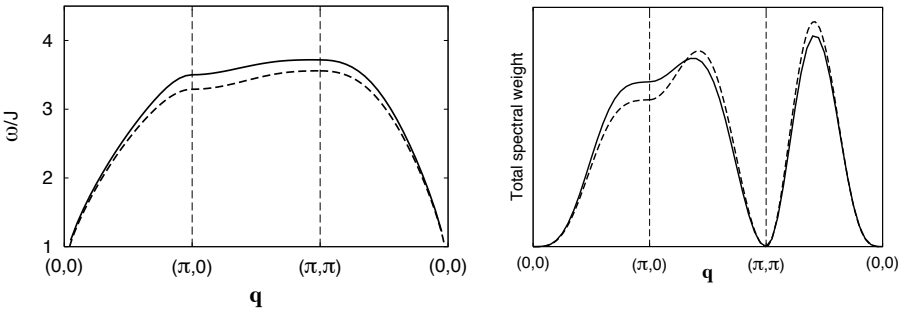


(a) (b)

**Figure 4.6:** (a) First moment and (b) total spectral weight of the RIXS spectrum. The solid lines are obtained by using interaction strengths determined from neutron data (next neighbor coupling $J = 146.3$ meV, second and third neighbor couplings $J' = J'' = 2$ meV and ring exchange $J_\square = 61$ meV) [83]. The dashed lines have only nearest neighbor interaction.

The vanishing of the RIXS intensity at $\mathbf{q} = \mathbf{0}$ is obvious: from Eq. (4.42) we see that at $\mathbf{q} = \mathbf{0}$, $\hat{O}_\mathbf{q}$ reduces to $2H_0$ (the factor of 2 arises from the fact that the sum in Eq. (4.42) is over all $i$ and $j$). At zero temperature, $|i\rangle = |0\rangle$ and consequently $H_0 |i\rangle = 0$ –the RIXS intensity vanishes. At nonzero temperatures, $H_0 |i\rangle = E_i |i\rangle$ and according to Eq. (4.41) only elastic scattering occurs. It is easy to show that at $\mathbf{q} = (\pi, \pi)$ the RIXS intensity always vanishes, regardless of the temperature or the form of $J_{ij}$. This holds because $\mathbf{q} = (\pi, \pi)$ is a reciprocal magnetic lattice vector: $e^{i\mathbf{q}\cdot\mathbf{R}_i} = 1$ if $\mathbf{R}_i$ is in sublattice $A$ and $e^{i\mathbf{q}\cdot\mathbf{R}_i} = -1$ if $\mathbf{R}_i$ is in sublattice $B$ (assuming that at $\mathbf{R}_i = (0, 0)$ we are in sublattice $A$). We obtain

$$\hat{O}_{\mathbf{q}=(\pi,\pi)} = \sum_{i\in A,j} J_{ij}\mathbf{S}_i\cdot\mathbf{S}_j - \sum_{i\in B,j} J_{ij}\mathbf{S}_i\cdot\mathbf{S}_j. \tag{4.47}$$

Adding all terms where $j \in B$ in the first term and $j \in A$ in the latter, we get zero. What remains is

$$\hat{O}_{\mathbf{q}=(\pi,\pi)} = \sum_{i,j\in A} J_{ij}\mathbf{S}_i\cdot\mathbf{S}_j - \sum_{i,j\in B} J_{ij}\mathbf{S}_i\cdot\mathbf{S}_j. \tag{4.48}$$

This operator commute with the Hamiltonian and therefore does not contribute to inelastic scattering.

The other remarkable feature of the magnetic RIXS spectrum is its strong dispersion. This is apparent from Fig. 4.5(a) and 4.6(a), showing the first moment (average peak position) of the spectrum. The calculations for the nearest neighbor Heisenberg antiferromagnet [see the dashed line in Fig. 4.6(a)] show that the magnetic scattering disperses from about $\omega \approx 0$ around $(0, 0)$ to $\omega \approx 4J$ at $(\pi, 0)$ and $(\pi/2, \pi/2)$. Longer range couplings tend to reduce (increase) the first

moment of the RIXS spectrum if they weaken (reinforce) the antiferromagnetic order [see the solid line in Fig. 4.6(a)]. The observed dispersion in Fig. 4.5(a) has a twofold origin. It is in part due to the **q**-dependence of the two-magnon density of states (DOS), combined with the scattering matrix elements that tend to pronounce the low energy tails of the two-magnon DOS. In Fig. 4.5(b), it looks as if the two-magnon DOS has two branches. The most energetic one around $\mathbf{q} = \mathbf{0}$ is strongly suppressed by the matrix elements throughout the Brillouin zone (BZ).

The consistency at $\mathbf{q} = (0, 0)$ and $\mathbf{q} = (\pi, \pi)$ of the theoretical results and experimental data was already noticed, but at other wave vectors, the agreement stands out even more. The data on $La_2CuO_4$ for $\mathbf{q} = (\pi, 0)$ shows a peak at around 500 meV, precisely where we find it on the basis of a nearest neighbor Heisenberg model with $J = 146$ meV – a value found by the analysis of neutron scattering data [83]. Similar agreement is found at $\mathbf{q} = (0.6\pi, 0)$ and $\mathbf{q} = (0.6\pi, 0.6\pi)$ [14]. Even better agreement is found when we take into account the second and third nearest neighbors and ring exchange according to the neutron data. The ring exchange interaction, which we treat on a mean field level, simply renormalizes first- and second-nearest neighbors exchange [83].

In Fig. 4.7, we compare the results for the two-magnon scattering intensity with experimental data [14], using the interaction strengths determined from neutron data [83], for three values of **q** in the BZ. Note that we use the wave vector independent renormalization factor $Z_c$ here, which takes into account some of the magnon-magnon interactions [104]. This simply changes the energy scale by a factor $Z_c \approx 1.18$ but does not affect the intensity of the spectrum. Each panel shows the theoretical prediction (dashed line), the theory convoluted with the current instrumental resolution (solid line), and the experimental data. The only free parameter in the theoretical spectra is the overall scale of the scattering intensity. We find it to vary by a factor of 2.5 comparing different **q**'s, which is within the error bars of the experiment [105].

Many qualitative features such as the occurrence of intense peaks at the magnetic BZ boundary and the large dispersion characterizing the total spectrum are in accordance with our earlier results [51] and the results of Nagao and Igarashi [96]. The spectra of Ref. [96], taking two-magnon interactions partially into account, show slight quantitative differences with respect to our results: the RIXS peaks soften and broaden somewhat as a consequence of the magnon-magnon interaction, particularly for the ($\pi$,0) point. The range of the dispersion in the spectrum is therefore smaller (the mean $\omega/J$ varies between 1 and 3 instead of 1 and 4).

**Finite *T*: single-magnon scattering.** The $S^z_{\mathrm{tot}}$ symmetry allows scattering processes where no additional magnons are created. In the finite temperature case, an initial magnon of momentum **k** can be scattered to $\mathbf{k} + \mathbf{q}$. The one-

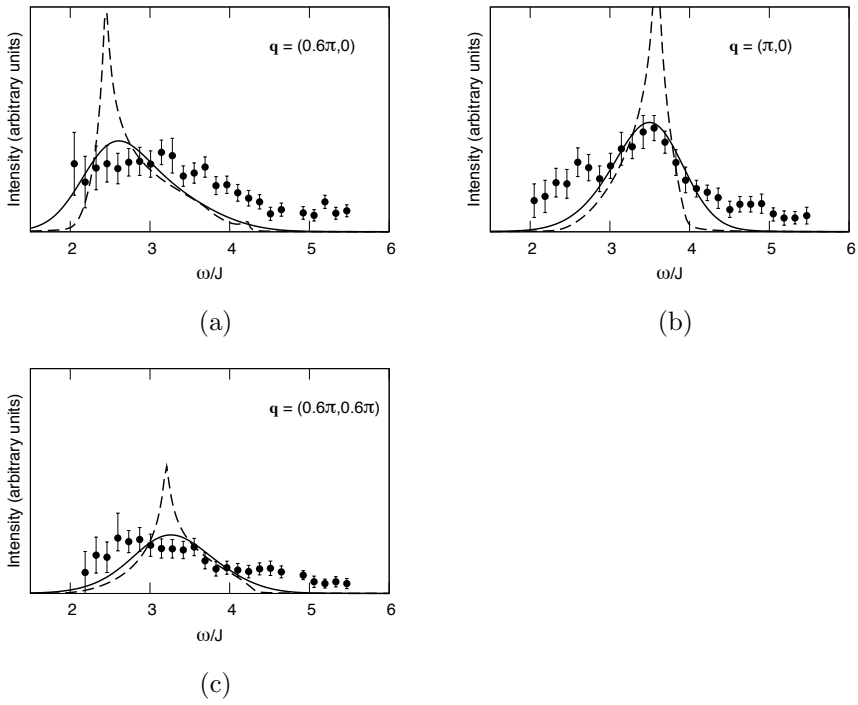


**Figure 4.7:** RIXS intensity for various points in the BZ. Each figure contains the bare theoretical data (dashed line), the convolution with experimental resolution (solid line), and the experimental data from Ref. [14]. For these figures, we used $J = 146.3$ meV, second and third neighbor couplings $J' = J'' = 2$ meV and ring exchange $J_\square = 61$ meV. The latter contribution is evaluated theoretically using a mean field approximation. These values were found in neutron scattering experiments [83]. These experiments were analyzed using the wave vector independent renormalization factor $Z_c = 1.18$, which is also used to generate the theoretical curves. The theoretical intensity is scaled independently in each figure to match the experiment. The overall scale factors differ at most by a factor 2.5, which is comparable to experimental uncertainty in absolute intensities [105].

magnon part of the scattering operator, within LSWT, takes the following form:

$$\hat{O}^{(1)}_{\mathbf{q}} = S \sum_{\mathbf{k}\in \mathrm{MBZ}} \Big[ \Big( J_{\mathbf{0}} + J_{\mathbf{q}} - J'_{\mathbf{0}} - J'_{\mathbf{q}} + J'_{\mathbf{k}} + J'_{\mathbf{k+q}} \Big) \Big( U_{\mathbf{k}} U_{\mathbf{k+q}} + V_{\mathbf{k}} V_{\mathbf{k+q}} \Big) - \Big( J_{\mathbf{k}} + J_{\mathbf{k+q}} \Big) \Big( U_{\mathbf{k}} V_{\mathbf{k+q}} + V_{\mathbf{k}} U_{\mathbf{k+q}} \Big) \Big] \Big( \alpha^\dagger_{\mathbf{k+q}} \alpha_{\mathbf{k}} + \beta^\dagger_{\mathbf{k+q}} \beta_{\mathbf{k}} \Big) . \tag{4.49}$$

We choose to concentrate on the basic case where the only non-vanishing interaction is the nearest-neighbors coupling $J$, for a 2D Heisenberg antiferromagnet with $S = 1/2$.

In the low temperature regime, a few magnons of low momentum $\mathbf{k}$ are present in the system. Their energy can be approximated for $T \to 0$ by letting $\mathbf{k} \to 0$: $\Omega_{\mathbf{k}} \approx \sqrt{2}J|\mathbf{k}|$. In this limit $U_{\mathbf{k}}$ and $V_{\mathbf{k}}$ can be substituted by the following approximate expressions:

$$\begin{aligned} U_{\mathbf{k}} &\approx \tfrac{1}{\sqrt{\sqrt{2}|\mathbf{k}|}}(1 + \tfrac{\sqrt{2}}{4}|\mathbf{k}|), \\ V_{\mathbf{k}} &\approx \tfrac{1}{\sqrt{\sqrt{2}|\mathbf{k}|}}(1 - \tfrac{\sqrt{2}}{4}|\mathbf{k}|). \end{aligned} \tag{4.50}$$

In order to calculate the one-magnon contribution to the cross section, we have to evaluate the scattering amplitude expressed by Eq. (4.41). In the low temperature case we can consider a one-magnon initial state $|i\rangle = \alpha^{\dagger}_{\mathbf{k}}|0\rangle$[1]. The only contribution to $\mathcal{F}^{(1)}_{fi}$ comes from the final state with a single magnon of momentum $\mathbf{k} + \mathbf{q}$

$$\begin{aligned} \mathcal{F}^{(1)}_{fi} &= S\left[(J_{\mathbf{0}} + J_{\mathbf{q}})(U_{\mathbf{k}}U_{\mathbf{k+q}} + V_{\mathbf{k}}V_{\mathbf{k+q}}) - (J_{\mathbf{k}} + J_{\mathbf{k+q}})(U_{\mathbf{k}}V_{\mathbf{k+q}} + V_{\mathbf{k}}U_{\mathbf{k+q}})\right] \\ &\approx \frac{S}{\sqrt{2\sqrt{2}}}\left(J_{\mathbf{0}} + J_{\mathbf{q}}\right)\left(U_{\mathbf{q}} - V_{\mathbf{q}}\right)\sqrt{|\mathbf{k}|} \end{aligned} \tag{4.51}$$

where we used the condition $|\mathbf{k}| \ll |\mathbf{q}|$ and inserted the expressions of Eqs. (4.50) for $U_{\mathbf{k}}$ and $V_{\mathbf{k}}$, retaining the leading order term in $|\mathbf{k}|$.

These approximations allow the analytic evaluation of the scattering intensity. At finite $T$, the cross section is given by

$$\left.\frac{d^2\sigma^{(1)}}{d\Omega d\omega}\right|_{\text{res}} \propto \sum_{i,f} \frac{1}{e^{\beta E_i} - 1}\left|\mathcal{F}^{(1)}_{fi}\right|^2 \delta(\hbar\omega - E_f + E_i). \tag{4.52}$$

For $\mathbf{k} \approx 0$, and by taking the continuum limit, we obtain

$$\frac{d^2\sigma^{(1)}}{d\Omega d\omega} \propto P(\mathbf{q}) \int_{\text{MBZ}} dk_x dk_y \frac{|\mathbf{k}|}{e^{\beta\Omega_{\mathbf{k}}} - 1}\delta(\hbar\omega - \Omega_{\mathbf{k+q}} + \Omega_{\mathbf{k}}), \tag{4.53}$$

where we defined $P(\mathbf{q}) = S^2\left(J_{\mathbf{0}} + J_{\mathbf{q}}\right)^2\left(U_{\mathbf{q}} - V_{\mathbf{q}}\right)^2$. In the low temperature limit, the Bose factor goes to zero rapidly for high $|\mathbf{k}|$, so the only substantial contribution to the integral comes from $|\mathbf{k}| \approx 0$. Therefore we can extend the domain of integration to the entire $k$ space. Replacing $\Omega_{\mathbf{k}}$ with its approximate expression in the limit of low $|\mathbf{k}|$, and assuming polar coordinates, we obtain

$$\frac{d^2\sigma^{(1)}}{d\Omega d\omega} \propto P(\mathbf{q}) \int_0^{\infty} dk \frac{k^2}{e^{\beta\sqrt{2}Jk} - 1}\delta(\hbar\omega - \Omega_{\mathbf{q}} + \sqrt{2}Jk) \tag{4.54}$$

[1] At finite temperature, more than one magnon can exist. This modifies the action of the $\hat{O}^{(1)}_{\mathbf{q}}$ operator in addition to the Bose factor. It is easy to show that, in the low temperature limit, the main contribution to this factor arises from $n_{\mathbf{k}} = 1$, since other terms rapidly go to zero for $\beta \to \infty$.

Note that we used the replacement $\Omega_{\mathbf{k}+\mathbf{q}} \to \Omega_{\mathbf{q}}$, which breaks down at $\mathbf{q} = \mathbf{0}$ and the BZ corners. This integral can simply evaluated to be

$$\frac{d^2\sigma^{(1)}}{d\Omega d\omega} \propto P(\mathbf{q}) \frac{(\hbar\omega - \Omega_{\mathbf{q}})^2}{e^{-\beta(\hbar\omega - \Omega_{\mathbf{q}})} - 1} \theta\left(\Omega_{\mathbf{q}} - \hbar\omega\right), \tag{4.55}$$

and the spectral weight for $T/J \ll 1$ is

$$W_1 = \int \frac{d^2\sigma^{(1)}}{d\Omega d\omega} d\omega \propto P(\mathbf{q}) \frac{1}{(\beta J)^3}. \tag{4.56}$$

The $T^3$ behavior also shows up in the numerical evaluation of $W_1$ (without assuming $|\mathbf{k}| \ll |\mathbf{q}|$), as shown in Fig. 4.8 as a function of the transferred momentum $\mathbf{q}$, for various temperatures (dashed lines). According to the considerations discussed in the previous section, the RIXS intensity is vanishing for $(\pi, \pi)$. The average peak position and the peak width are expected to be modified as a function of temperature. We can easily estimate these modifications by evaluating the first moment

$$\langle \hbar\omega_{\max} \rangle \approx \Omega_{\mathbf{q}} - \frac{\pi^4}{30\zeta(3)} T, \tag{4.57}$$

and the variance

$$\langle \hbar\omega_{\max} \rangle^2 - \langle \hbar\omega_{\max} \rangle^2 \propto T^2. \tag{4.58}$$

We conclude that the peak position is shifted from $\Omega_{\mathbf{q}}$ towards lower values of $\hbar\omega$, by an amount that grows linearly with $T$ and at the same time the peak broadens proportional to $T$.

We now determine the relative intensity of the one- and two-magnon scattering processes. Even if a direct comparison is not possible, since the one-magnon and the two-magnon peaks occur at different lost energies $\hbar\omega$, it is useful to compare the one-magnon and the two-magnon total spectral weight for the 2D Heisenberg antiferromagnet. The latter is evaluated numerically at $T = 0$, and the former at various temperatures without making the approximation $\mathbf{k}+\mathbf{q} \approx \mathbf{q}$. In Fig. 4.8 we plot the two-magnon (solid line) and the one-magnon weight for different temperatures (dashed lines). At room temperature, the one-magnon weight is one or two orders of magnitude smaller for almost every value of $\mathbf{q}$ and is expected to decrease with decreasing $T$, according to Eq. (4.56). This allows us to conclude that the two-magnon scattering is the dominant process at low temperatures. A rough estimate for the temperature at which the one-magnon process becomes significant gives a value of $\sim$ 1 eV in the case of $La_2CuO_4$, which is well above room temperature. These results support the conclusion that two-magnon scattering dominates the magnetic RIXS intensities in this material observed by Hill *et al.* [14] and Ellis *et al.* [53]. In other materials this of course needs not necessarily be so, depending on the temperature at which the experiments are performed. One can expect for instance interesting RIXS scattering signals from high temperature paramagnons.

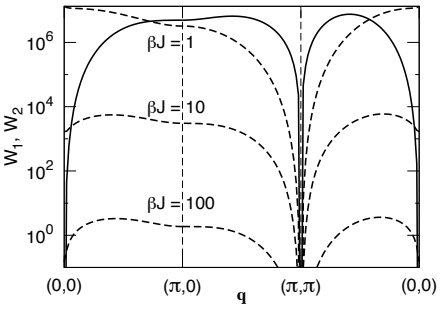


**Figure 4.8:** Comparison between spectral weight for single-magnon scattering $W_1$ (dashed lines) for various temperatures and zero temperature two-magnon scattering $W_2$ (solid line), all obtained numerically. The vertical scale has arbitrary units. $W_1$ displays the $T^3$ behavior from Eq. (4.56) for the single-magnon intensity. For $La_2CuO_4$, $J \approx 146$ meV, and at room temperature we have $\beta_{\rm rt} J \approx 5.8$.

**Leading correction to ultrashort lifetime approximation.** The UCL expansion offers a systematic way of calculating the Kramers-Heisenberg equation. In this section we calculate the leading correction term to the two-magnon cross section in the UCL approximation. This is especially relevant at $\mathbf{q} = (0, 0)$ where the intensity is vanishing to first order, but non-zero to second order. The leading order correction is taken into account by including all terms up to $\mathcal{O}((\eta J/\Gamma)^2)$ in Eq. (4.40). Again we can include a number of extra correction terms by using an expansion of the type

$$\sum_{l=1}^{\infty} \frac{H_{\rm int}^l}{(i\Gamma)^l} \approx \sum_{l=1}^{\infty} \left( \frac{H_0^l}{(i\Gamma)^l} + \frac{H_0^{l-1} H'}{(i\Gamma)^l} \right) + \sum_{l=2}^{\infty} \frac{H_0^{l-2} (H')^2}{(i\Gamma)^l} + \mathcal{O}\left((\eta J/\Gamma)^3\right). \quad (4.59)$$

The contribution of the last term to the UCL scattering amplitude is

$$\frac{1}{\Gamma^2} \frac{\eta^2}{\hbar\omega - i\Gamma} \langle f | \sum_i e^{i\mathbf{q}\cdot\mathbf{R}_i} \sum_{j,k} J_{ij} J_{ik} (\mathbf{S}_i \cdot \mathbf{S}_j)(\mathbf{S}_i \cdot \mathbf{S}_k) | i \rangle \quad (4.60)$$

This scattering amplitude that corresponds to this term is non-zero at $\mathbf{q} = \mathbf{0}$, which can be easily checked in linear spin wave theory. The reason is that the resulting scattering operator at zero transferred momentum does not commute with the Hamiltonian. For the LSW analysis, we make use of the identity

$$\sum_{j,k} J_{ij} J_{ik} (\mathbf{S}_i \cdot \mathbf{S}_j)(\mathbf{S}_i \cdot \mathbf{S}_k) = \frac{1}{4} \sum_{j \neq k} J_{ij} J_{ik} \mathbf{S}_j \cdot \mathbf{S}_k - \frac{1}{2} \sum_j J_{ij}^2 \mathbf{S}_i \cdot \mathbf{S}_j + \text{const.} \quad (4.61)$$

We drop the constant because it does not contribute to inelastic scattering. For simplicity, we only take nearest neighbor interactions into account. The last term in Eq. (4.61) is proportional to the first order result for the scattering amplitude, which has already been analyzed in LSWT. The other term can be treated in LSWT too and yields a two-magnon contribution to the scattering amplitude at zero temperature of:

$$-\frac{1}{4\Gamma^2} \frac{(\eta J)^2}{\hbar\omega - i\Gamma} \sum_{\mathbf{k}} \langle f | f(\mathbf{k}, \mathbf{q}) (U_{\mathbf{k}} V_{\mathbf{k}-\mathbf{q}} + U_{\mathbf{k}-\mathbf{q}} V_{\mathbf{k}}) \alpha_{\mathbf{k}}^\dagger \beta_{-\mathbf{k}+\mathbf{q}}^\dagger | 0 \rangle \quad (4.62)$$

with $f(\mathbf{k},\mathbf{q}) = -6(\cos q_x + \cos q_y) + 4\cos k_x \cos(k_y - q_y) + 4\cos k_y \cos(k_x - q_x) + 2\cos(2k_x - q_x) + 2\cos(2k_y - q_y)$. Since the phase of the first order amplitude differs from the second order amplitude by $\pi/2$, there is no interference of these terms. The consequence is that the leading corrections to the first order scattering intensity are down by a factor $(\eta J/\Gamma)^2 \approx 0.06$ for the well-screened intermediate state. This makes the UCL expansion a viable way of computing magnetic RIXS spectra. The contribution Eq. (4.60) is shown in Fig. 4.9(a), and the full cross section in Fig. 4.9(b). Only at $\mathbf{q} = \mathbf{0}$, there is an appreciable difference from the first order result shown in Fig. 4.5 (a). At $\mathbf{q} = (\pi, \pi)$, there is again no intensity, which can be understood by the same argument as for the first order result in Sec. 4.4.

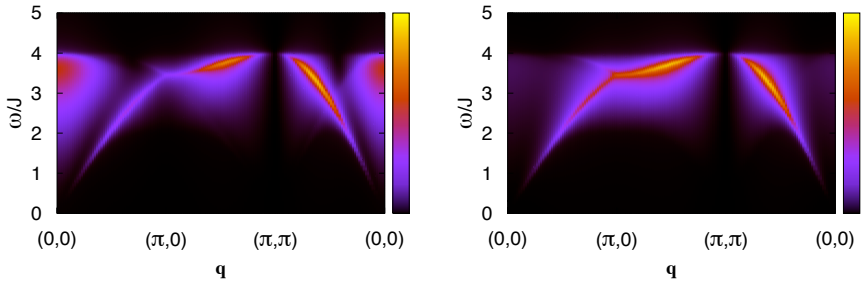


**Figure 4.9:** The leading order correction to the scattering amplitude does not interfere with the first order. Fig. (a) shows the contribution to the cross section from Eq. (4.60). The full, corrected cross section is shown in Fig. (b). There is an appreciable correction only at $\mathbf{q} = \mathbf{0}$.

**Comparison to two-magnon Raman scattering.** In Raman scattering, one can select the symmetry of the two-magnon mode by selecting a certain polarization configuration. The Loudon-Fleury Raman scattering operator is [106–108]

$$\hat{O}_{\mathrm{LF}} \propto \sum_{i,\delta} P(\delta)\mathbf{S}_i \cdot \mathbf{S}_{i+\delta}. \tag{4.63}$$

The polarization configuration determines the symmetry of the scattering operator through $P(\delta) = (\boldsymbol{\delta} \cdot \boldsymbol{\epsilon}')(\boldsymbol{\delta} \cdot \boldsymbol{\epsilon})$. In two-magnon RIXS at the Cu K edge, in contrast, the polarization dependence can be disentangled from the scattering operator, and the polarization cannot be used to select the symmetry of the excitations one probes. However, RIXS has momentum dependence, with which one can obtain the same effect: the role of $P(\delta)$ is taken over by the phase factor $e^{i\mathbf{q}\cdot\mathbf{R}_i}$ in RIXS: compare Eq. (4.42) for nearest neighbors to Eq. (4.63). RIXS can also select two-magnon modes of different symmetry by tuning to specific $\mathbf{q}$'s.

The simplest case is that of $A_{1g}$ symmetry [*i.e.*, $P(\delta)$ transforms as $A_{1g}$ under the symmetry operations of $D_{4h}$, so $P_{A_{1g}}(\delta) = 1$], which corresponds to RIXS at $\mathbf{q} = \mathbf{0}$, so $e^{i\mathbf{q}\cdot\mathbf{R}_i} = 1$. In this case, both Raman and RIXS do not show inelastic weight (in theory).

For the less trivial symmetries, we rewrite the RIXS phase factor as:

$$\hat{O}_{\mathbf{q}} \propto \sum_{i,\delta} e^{i\mathbf{q}\cdot\mathbf{R}_i}\mathbf{S}_i \cdot \mathbf{S}_{i+\delta} = \sum_{i,\delta} \frac{1}{2} e^{i\mathbf{q}\cdot\mathbf{R}_i}(1 + e^{i\mathbf{q}\cdot\boldsymbol{\delta}})\mathbf{S}_i \cdot \mathbf{S}_{i+\delta}. \tag{4.64}$$

The phase factor on the right-hand side is now symmetric under the exchange of neighbors $i$ and $i + \delta$. To probe the $B_{2g}$ two-magnon mode (which transforms as $xy$), one needs

$$\frac{1}{2} e^{i\mathbf{q}\cdot\mathbf{R}_i}(1 + e^{i\mathbf{q}\cdot\boldsymbol{\delta}}) = P_{B_{2g}}(\boldsymbol{\delta}) = 0, \tag{4.65}$$

which is satisfied for all $\mathbf{R}_i$ at $\mathbf{q} = (\pi, \pi)$. Indeed, both RIXS and Raman scattering predict zero intensity for a nearest neighbor Heisenberg antiferromagnet.

For $B_{1g}$ symmetry ($x^2$-$y^2$), the RIXS phase factor must satisfy impossible conditions:

$$\text{const.} \times e^{i\mathbf{q}\cdot\mathbf{R}_i}(1 + e^{\pm i\mathbf{q}\cdot\hat{x}}) = P_{B_{1g}}(\pm\hat{\mathbf{x}}) = +1 \tag{4.66}$$

$$\text{const.} \times e^{i\mathbf{q}\cdot\mathbf{R}_i}(1 + e^{\pm i\mathbf{q}\cdot\hat{y}}) = P_{B_{1g}}(\pm\hat{\mathbf{y}}) = -1. \tag{4.67}$$

The first condition implies $q_y = 0$, which is incompatible with the second one. Thus, Cu K edge RIXS cannot probe the $B_{1g}$ two-magnon mode.

The only other wave vector for RIXS that we might expect to be special is $\mathbf{q} = (\pi, 0)$, but this leads to a mode that is not symmetric under, for example, rotations over 90° and therefore cannot be classified as a representation of the symmetry group $D_{4h}$.

We conclude that indirect RIXS on a nearest neighbor Heisenberg antiferromagnet can probe two-magnon excitations of a certain symmetry by choosing an appropriate $\mathbf{q}$, instead of choosing the polarization as in Raman scattering. Unfortunately, this is only possible for the $A_{1g}$ and $B_{2g}$ cases, which give no inelastic weight for both Raman and RIXS spectra, at least in theory. Comparison of any residual two-magnon feature in experimental RIXS and Raman spectra (resulting from, *e.g.*, longer range interactions [109]) is not necessarily expected to show agreement.

**Conclusions.** We derived the two-magnon scattering cross section which is measured in magnetic RIXS at the Cu K edge, taking advantage of a series expansion in the UCL of the intermediate state. In the context of LSWT, we calculated the magnetic RIXS spectrum for a 2D $S = 1/2$ Heisenberg antiferromagnet, in the more general case where the superexchange is not limited to nearest neighbors. Our results strongly suggest a multi-magnon scattering scenario, where two-magnon excitations are created in the system as a consequence

of the modifications in the superexchange interaction induced by the core hole potential.

Our results for the two-magnon scattering agree very well with experimental data on $La_2CuO_4$. The vanishing of the RIXS intensity for the elastic case $\mathbf{q} = (0, 0)$ and the antiferromagnetic point $\mathbf{q} = (\pi, \pi)$ is recovered. The latter feature turns out to be a consequence of an underlying symmetry property of the scattering operator and does not depend on the range of the exchange interaction. The excellent quantitative agreement between our results and experiments is testified by the occurrence of an intense peak at $\mathbf{q} = (\pi, 0)$ for $\hbar\omega \approx 500$ meV. We have generalized the theory to include also finite temperature scattering, for which we find that also one-magnon processes contribute. For $La_2CuO_4$ at room temperature, the single-magnon spectral weight is very small compared to two-magnon scattering.

The subleading order in the UCL expansion of the cross section is shown to be of order $\mathcal{O}((\eta J/\Gamma)^2)$ smaller than the first order result. This makes the expansion a rigorous method for this case to calculate the Kramers-Heisenberg relation. The introduction of longer range interactions (according to data from neutron experiments) improves the correspondence between theory and magnetic RIXS experiments on $La_2CuO_4$. The generalization of the analysis to doped systems will be an interesting next step towards understanding multi-spin correlations in the spin liquid phase of the high-$T_c$ superconductors.

**Acknowledgments.** We thank Michel van Veenendaal for stimulating discussions and John P. Hill for also sharing unpublished data with us. We gratefully acknowledge support from the Argonne National Laboratory Theory Institute, Brookhaven National Laboratory (DE-AC02-98CH10996) and the Dutch Science Foundation FOM. This paper was supported in part by the National Science Foundation under Grant No. PHY05-51164.

## 4.5 Copper L edge

### 4.5.1 Theory of probing single magnons in cuprates with RIXS

Published as '*Theoretical Demonstration of How the Dispersion of Magnetic Excitations in Cuprate Compounds can be Determined Using Resonant Inelastic X-Ray Scattering*' in Phys. Rev. Lett. **103**, 117003 (2009) with Giacomo Ghiringhelli, Marco Moretti Sala, Lucio Braicovich, and Jeroen van den Brink.

**Abstract.** *We show that in Resonant Inelastic X-ray Scattering at the copper L and M edge direct spin flip scattering is in principle allowed. We demonstrate how this possibility can be exploited to probe the dispersion of magnetic excitations, for instance magnons, of cuprates such as the high-$T_c$ superconductors. We*

*compute the relevant local and momentum dependent magnetic scattering amplitudes, which we compare to the elastic and dd excitation scattering intensities. For cuprates these theoretical results put RIXS as a technique on the same footing as neutron scattering.*

**Introduction.** Here we show that contrary to common belief [2, 72, 73, 110], RIXS at the copper L edge is also a powerful probe of single spin flip excitations and related magnetic dispersions. The presence of this magnetic scattering channel is an important theoretical result because it puts L edge RIXS on, for instance, the high-$T_c$ superconductors, as a technique on the same footing as neutron scattering.

Soft X-ray RIXS has been much used in transition metal oxides to study local transitions, such as dd excitations in cuprates [9,73,110] and spin flips [111,112] in NiO. Although interesting in themselves, these experiments do not exploit a unique capability of RIXS: to measure the *dispersion* of excitations by determining both momentum change and energy loss of the scattered X-ray photons. This capability is far beyond the possibilities of traditional low energy optical techniques, which are constrained to essentially zero momentum transfer because, as opposed to high energy X-rays, photons in the visible range carry negligible momentum. This asset of RIXS has already been exploited to determine the momentum dependence of charge [85, 86], bimagnon [14, 51, 52, 96] and orbital excitations [54] at Cu K and $L_3$ edges.

In order to prove that at the Cu L edge RIXS can probe dispersion of collective magnetic excitations, we will first determine the local spin flip cross section for a copper $d^9$ ion in a tetragonal crystal field. This is the familiar case encountered in numerous cuprates, with one hole occupying the $x^2$-$y^2$ orbital. The important observation is that the local spin flip process can either be forbidden or allowed, depending on the spatial orientation of the copper spin. Subsequently, we calculate the momentum ($\mathbf{q}$) dependence of the magnon cross section for a spin system with a collective response. As an example we consider the Heisenberg antiferromagnet, where we find a vanishing of the magnon scattering intensity around the center of the Brillouin zone proportional to $|\mathbf{q}|$ and a strong peak at the antiferromagnetic wave vector.

**Local spin flip scattering at Cu L edge.** From the viewpoint of inelastic magnetic scattering, RIXS and neutron scattering appear to be very different techniques. It is easy to show, for instance, that in transition metal K edge RIXS single spin flip scattering is forbidden [51] because of the absence of spin orbit coupling in the intermediate state. Ever since the seminal work of Kuiper and coworkers [110], more than a decade ago, it is believed that also at the copper L and M edge spin flip scattering is not allowed for $Cu^{2+}$ in a tetragonal crystal field, unless the spin flip excitation is accompanied by a dd excitation [2,72,73]. Based on a symmetry analysis of the wavefunction of the copper hole, Ref. [72] concludes

that "the reason is that the $x^2$-$y^2$ state, a linear combination of atomic $Y_{2,2}$ and $Y_{2,-2}$ states, does not allow a direct spin flip transition." The observation that the spin flip excitations are intrinsically entangled with dd excitations implies that mapping out momentum dependencies of magnetic excitations with L edge RIXS would be a hopeless endeavor. As will be clarified shortly, the dd-excitations act as a momentum sink, which would limit the information that can be gained from RIXS in this case to *momentum averaged properties* of the magnetic excitations, preempting the possibility to observe, *e.g.*, a single magnon dispersion.

We will show in the following, however, that the symmetry analysis on which these assertions rely [72, 73] is incomplete because it is restricted to directions of the spin moment along an axis that is orthogonal to the $x^2$-$y^2$ orbital. In fact we will show that for any other spin orientation direct spin flip scattering is allowed. This includes, in particular, Néel ordered cuprates, where the magnetic moment lies in the plane of the $x^2$-$y^2$ orbital: for example, in $La_2CuO_4$, $Sr_2CuO_2Cl_2$ and $(CaSr)CuO_2$ [113, 114], spins order along the $[x, y, z]$=[110] direction and in $Nd_2CuO_4$ along [100] and [010] in alternating planes [115].

The dependence of the direct spin flip scattering amplitude on photon polarization, scattering angle and momentum transfer can be computed from the Kramers-Heisenberg expression (2.41). At the copper L edge we are dealing with the local electronic process $2p^6 3d^9 \rightarrow 2p^5 3d^{10} \rightarrow 2p^6 3d^{9*}$, where $*$ denotes an excited state with a dd excitation and/or spin flip. At the $L_3$ resonance the intermediate states $|n\rangle$ are just the multiplets corresponding to the four $J^z = L^z + S^z$ states of the spin-orbit coupled $2p_{3/2}$ core hole.

It is easy to see that direct spin flip excitations are forbidden if the spin of the hole in the $x^2$-$y^2 \propto (Y_{2,2} + Y_{2,-2})/\sqrt{2}$ initial state is aligned along [001], which is the situation considered previously [72, 73]. In the first step of the RIXS process a dipole allowed $2p \rightarrow 3d$ transition creates a core hole in a linear combination of $Y_{1,1}$ and $Y_{1,-1}$, while conserving the spin. In this intermediate state the spin-orbit coupling of the core hole $\mathbf{L} \cdot \mathbf{S} = L^z S^z + (L^+ S^- + L^- S^+)/2$ can cause a spin flip $S^-$ (or $S^+$) in combination with a raising (or lowering) $L^+$ (or $L^-$) of the orbital moment. In either case a $Y_{1,0}$ core hole state with reversed spin is the result [72, 73, 116]. The last step to end up in a final state with only a spin flip excitation, requires the optical decay of the $Y_{1,0}$ 2p core hole into a $(Y_{2,2} + Y_{2,-2})/\sqrt{2}$ 3d valence band hole. But this transition is dipole forbidden because it requires $\Delta L^z = 2$, which thus forbids direct spin flip scattering.

The situation changes drastically when the local magnetic moment is oriented in the $xy$ plane: we will show that in this case direct spin flip excitations are fully allowed. This is best illustrated by a direct calculation of the RIXS amplitudes in the different channels for $Cu^{2+}$ in a tetragonal crystal field. We consider a scattering geometry as in Fig. 4.10(a), with fixed scattering angle of 90° and $\pi$ ($\sigma$) linear polarization of the incident photons parallel (perpendicular) to the scattering plane. In this geometry $\theta_{\mathrm{IN}}$ is the azimuthal angle between incident beam and [001] axis. In Fig. 4.10(b) we show the polarization and momentum dependent RIXS matrix elements to all possible final states for the starting con-

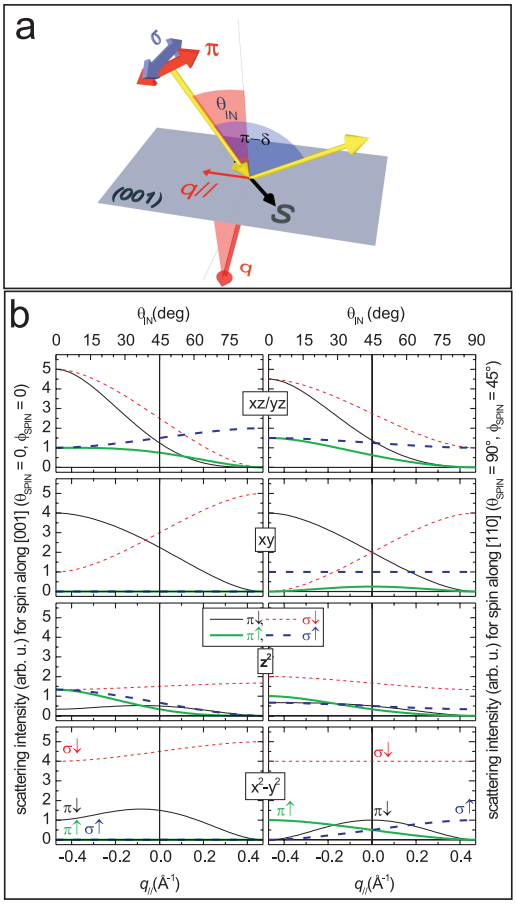


**Figure 4.10:** $L_3$ RIXS cross section for a single $Cu^{2+}$ ion with $\sigma$ and $\pi$ polarization of the incident beam. (a) The geometry: the scattering plane is (100), scattering angle 90°, the incident photons impinge at an angle $\theta_{\rm IN}$ to the [001] direction ($c$ axis). (b) Scattering intensities to different orbital and spin orientations, starting from a $(x^2\text{-}y^2)\downarrow_z$ state (left panels) and a $(x^2\text{-}y^2)\downarrow_{xy}$ groundstate (right panels) as a function of $\theta_{\rm IN}$ or alternatively the in-plane transferred momentum $q_\parallel$. For $\downarrow_z$, *i.e.*, spin along [001], the spin flip cross section vanishes (bottom left), not so for $\downarrow_{xy}$, with spin along [110] (right).

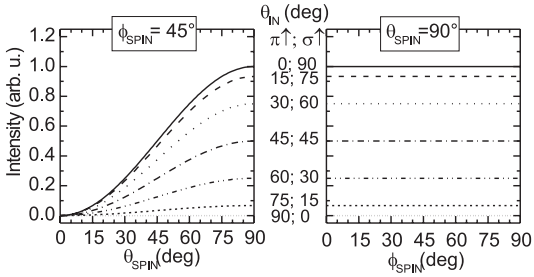


**Figure 4.11:** The dependence of scattering cross section for spin flip scattering to $(x^2\text{-}y^2)\uparrow$ final states on the atomic spin orientation for selected cases of scattering geometry given by varying $\theta_{\rm IN}$ and fixed $\phi_{\rm IN} = 0$.

figuration of a hole in the $x^2$-$y^2$ orbital with a spin oriented either along [001] (left panels) or along [110] (right panels), denoted by $(x^2\text{-}y^2)\downarrow_z$ and $(x^2\text{-}y^2)\downarrow_{xy}$, respectively, so that $(x^2\text{-}y^2)\uparrow$ is a final state with only a spin flip excitation.

Note that along the [100] direction the nuclear Brillouin zone boundary is in $q_\parallel \approx 0.826$ Å$^{-1}$ for $a = 3.8$ Å an in-plane lattice parameter that is typical for cuprates. At 90° scattering Cu $L_3$ RIXS can explore half of the reciprocal space, but going to backscattering geometry $q_\parallel$ grows considerably and almost all the Brillouin zone can be covered. Fig. 4.10(b) shows that the spin flip to dd excitation intensity ratio varies from zero at the zone center to about 0.1 at the zone edge. From the lower panels in Fig. 4.10 at the left and right it is clear that for a spin along [110] the spin flip cross section is allowed for both $\sigma$ and $\pi$ polarizations, whereas it is in all cases forbidden for a spin along [001]. It is interesting to note that for the $\sigma$ polarization the elastic peak is more than 4 times stronger than the spin flip scattering channel, whereas for $\pi$ the two intensities are similar. The direct spin flip cross section for a generic spin direction, characterized by the Euler angles $(\theta_{\rm spin}, \phi_{\rm spin})$ is shown in Fig. 4.11 for a number of azimuthal angles $\theta_{\rm IN}$.

The upshot of these numerical results can easily be understood on the basis of a symmetry argument. If the spin of the $x^2$-$y^2$ hole points along the $x$ axis, it is in the spin state $(|\uparrow\rangle + |\downarrow\rangle)/\sqrt{2}$, corresponding to $S^x = 1/2$. In the intermediate $2p_{3/2}$ core hole state the diagonal part of the spin-orbit coupling, $L^zS^z$, causes a transition of this spin state into $(|\uparrow\rangle - |\downarrow\rangle)/\sqrt{2}$ (corresponding to $S^x = -1/2$), while the angular part of the core hole wavefunction stays in a linear combination of $Y_{1,1}$ and $Y_{1,-1}$. The transition of the core hole back into the 3d $x^2$-$y^2$ orbital is therefore dipole allowed while at the same time the spin along the $x$ axis is flipped.

**Momentum dependence of magnon cross section.** We now wish to generalize the cross section from local spin flips to collective magnetic excitations, which are characterized by their momentum quantum number $\mathbf{q}$. There are several ways to compute the $\mathbf{q}$ dependence of this cross section, but a particularly transparent one is by the UCL expansion (2.49), which we will employ to zeroth order. This corresponds with summing over only the $J = 3/2$ core states in the

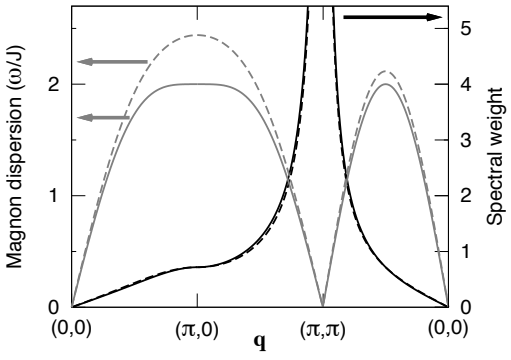


**Figure 4.12:** Momentum dependence of the magnetic RIXS spectral weight at the Cu $L_3$ edge (black) and the magnon dispersion (gray) for a simple 2D Heisenberg model (solid curves) and an extended model relevant for $La_2CuO_4$ [83] (dashed).

sum over intermediate states. The dipole operators $\mathcal{D}$ and $\mathcal{D}'^{\dagger}$ now allow for a direct creation of a spin flip upon de-excitation. The corresponding amplitude $T_{\mathrm{sf},L_3}(\boldsymbol{\epsilon}', \boldsymbol{\epsilon})$ depends on incident and outgoing polarization, as clarified above and shown in Figs. 4.10 and 4.11. We thus obtain

$$\mathcal{F}_{fg} = \frac{1}{i\Gamma} \sum_{L_3} T_{\mathrm{sf},L_3}(\boldsymbol{\epsilon}', \boldsymbol{\epsilon}) \sum_i e^{i\mathbf{q}\cdot\mathbf{R}_i} \langle f| \sigma_i^z |g\rangle \tag{4.68}$$

where the operator $\sigma^z$ flips the spin when it is in the $xy$ plane. The sum is over all intermediate core hole states of the $L_3$ edge, and we denote the shorthand $T_{\mathrm{sf}}(\boldsymbol{\epsilon}', \boldsymbol{\epsilon}) = \sum_{L_3} T_{\mathrm{sf},L_3}(\boldsymbol{\epsilon}', \boldsymbol{\epsilon})$.

It is instructive to compute with this generic expression the single magnon RIXS spectrum for an antiferromagnetic 2D Heisenberg model, given by Eq. 4.1. Rotating the spin operators to align the staggered magnetization along the $z$ axis, introducing Holstein-Primakoff bosons and adopting linear spin wave theory one finds after a Fourier and a Bogoliubov transformation the magnon scattering amplitude

$$\mathcal{F}_{fg} = \sqrt{N} \frac{1}{i\Gamma} T_{\mathrm{sf}}(\boldsymbol{\epsilon}', \boldsymbol{\epsilon})(u_{\mathbf{q}} - v_{\mathbf{q}}) \langle f| \alpha_{-\mathbf{q}} + \alpha_{\mathbf{q}}^{\dagger} |g\rangle \tag{4.69}$$

with $N$ the total number of sites. The resulting zero-temperature single magnon spectrum,

$$\frac{d^2\sigma}{d\Omega d\omega} \propto \left|T_{\mathrm{sf}}(\boldsymbol{\epsilon}', \boldsymbol{\epsilon})\right|^2 (u_{\mathbf{q}} - v_{\mathbf{q}})^2 \delta(\omega - \omega_{\mathbf{q}}), \tag{4.70}$$

is shown in Fig. 4.12. At $\mathbf{q} = (0, 0)$ the magnon scattering amplitude vanishes because in this situation the scattering operator is proportional to the total spin in the $z$ direction $S^z_{\mathrm{tot}}$, which does not cause inelastic processes because this operator commutes with the Heisenberg Hamiltonian. For small transferred momenta, $|\mathbf{q}| \to 0$, the magnon scattering intensity vanishes as $\omega_{\mathbf{q}}/4J$. We also observe that the magnon cross section diverges at $\mathbf{q} = (\pi, \pi)$ as $4J/\omega_{\mathbf{q}}$, similar to the neutron scattering form factor. This divergence is due to the RIXS photons scattering

on spin fluctuations: at $\mathbf{q} = (\pi, \pi)$ the scattering operator is proportional to the staggered spin along the $z$ axis $S^z_{\text{stag}}$, so that the total, energy integrated, scattering intensity $\int d\omega \sum_f |\mathcal{F}_{fg}|^2 \delta(\hbar\omega - E_f) \propto \left\langle (S^z_{\text{stag}})^2 \right\rangle$ and the inelastic scattering intensity is proportional to the variance $\left\langle (S^z_{\text{stag}})^2 \right\rangle - \left\langle S^z_{\text{stag}} \right\rangle^2$. We performed the same calculation for a Hamiltonian including longer-range and ring exchange terms, with a parameterization derived from neutron scattering[2]. Fig. 4.12 shows that these additional interactions cause only small changes in the momentum dependence of the magnetic scattering cross section.

Using the same formalism, we can compute the $\mathbf{q}$ dependent scattering amplitude of a spin flip entangled with a dd excitation. If the local spin flip operator is $S^-_i$ and the operator corresponding to the dd transiton is $T^+_i$, the inelastic scattering amplitude is $\mathcal{F}_{fg} \propto \langle f | \sum_i e^{i\mathbf{q}\cdot\mathbf{R}_i} S^-_i T^+_i | g \rangle = \langle f | \sum_{\mathbf{k}} S^-_{\mathbf{k}} T^+_{\mathbf{k}-\mathbf{q}} | g \rangle$. Clearly part of the momentum is absorbed by the dd excitation, so that RIXS measures a momentum convolution of the two excitations. In particular, the magnetic scattering amplitude looses all $\mathbf{q}$ dependence if the dd excitation is dispersionless, exemplifying that in order to determine magnon dispersions the presence of a *direct* spin flip process is essential.

**Conclusions.** Depending on the spatial orientation of the copper spin, the local spin flip process for RIXS at the $L_3$ edge can be forbidden or allowed. This makes RIXS a very sensitive probe of the orientation of the local magnetic moment. In typical cuprates direct spin flip scattering is allowed and for this case we determined the spin flip and magnon cross section, which turns out to be strongly momentum and polarization dependent. Our theory holds at both the copper L and M edges. At the M edge ($\hbar\omega_{\mathbf{k}} \approx 75$eV) the photon momentum is small, so that only magnons in a very small portion of the Brillouin zone can be probed. But at the copper $L_3$ edge the X-ray photon carries a momentum $|\mathbf{q}_{\text{in}}| \sim 0.47$ Å$^{-1}$, which is in a typical cuprate large enough to observe magnetic excitations in almost all of the Brillouin zone. Indeed very recently high resolution soft X-ray RIXS experiments on $La_2CuO_4$ have for the first time resolved the single magnon dispersion, confirming our predictions [11,21]. Thus, at least for high-$T_c$ superconductors, L edge RIXS can be placed on the same footing as neutron scattering – with the additional great advantage that for photon scattering only small sample volumes are required so that the measurement of the spin dynamics of thin films, oxide heterostructures and other nanostructures comes now within experimental reach.

**Acknowledgments.** We thank Michel van Veenendaal, Tom Devereaux, Maurits Haverkort, Marco Grioni and George Sawatzky for stimulating discussions. This research benefited from the RIXS collaboration supported by the Computational Materials Science Network (CMSN) program of the Division of Materials

[2]Next-nearest neighbor $J'/J = -0.11$, next-next-nearest neighbor $J''/J = 0.026$ and ring exchange $J_\square/J = 0.41$ [83]

Science and Engineering, U. S. Department of Energy, grant number DE-FG02-08ER46540 and is supported by the Dutch Science Foundation FOM.

### 4.5.2 Experimental verification of the single magnon theory

Soon after the predictions of Ref. [19] for the single magnon cross section, the single magnon dispersion was measured by Braicovich *et al.* [11]. A typical RIXS spectrum is shown in Fig. 4.13, together with the dispersion found by the authors. The dispersion is obtained by tracing the peak of the low energy spectrum along the [100] direction. The agreement with the dispersion obtained by neutron scattering is excellent.

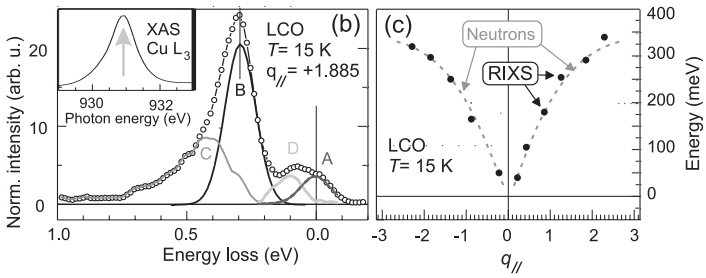


**Figure 4.13:** Left panel: a typical low energy RIXS spectrum of 2D cuprates. Shown here is a spectrum at the Cu $L_3$ edge of $La_2CuO_4$ at $\mathbf{q} = (0.6\pi, 0)$. The spectrum is decomposed in (A) the elastic peak, (B) a single magnon peak (by fitting a Gaussian at the spectrum's maximum), leaving (C) multiple magnon modes at higher energy and (D) optical phonons at lower energy. In the inset the $L_3$ X-ray Absorption Spectrum is shown, where the arrow indicates excitation energy. Tracing the maximum of the RIXS spectra at different transferred momenta along the [100] direction, RIXS can determine the single magnon dispersion, as shown in the right panel. The black dots were found by RIXS experiments [11] and the dashed, gray line by inelastic neutron scattering [83]. All RIXS measurements were done at $T = 15$ K. Figures from Ref. [11].

More data was taken by Guarise *et al.* [69], who also used the Cu $L_3$ edge. Their data are shown and compared to theory in Fig. 4.14. They are consistent with the results from inelastic neutron scattering on $La_2CuO_4$ [83], and cover for the first time the full dispersion in $Sr_2CuO_2Cl_2$ up to the boundary of the magnetic Brillouin zone. They reveal a striking 70 meV difference between the magnon energies of 310 meV at $(\pi, 0)$ and 240 meV at $(\pi/2, \pi/2)$, suggesting that further neighbor interactions are important. The large disersion along the magnetic Brillouin zone boundary can be compared with the smaller $\sim 20$ meV dispersion in $La_2CuO_4$ [83]. The dispersion along the magnetic zone boundary

is also predicted by recent LDA+U theory, which, however, underestimates the energy at $\mathbf{q} = (\pi, 0)$ in $Sr_2CuO_2Cl_2$ by almost 50 meV [117].

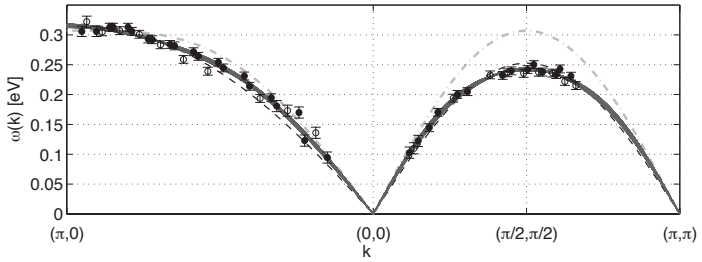


**Figure 4.14:** Single magnon dispersion measured at the Cu $L_3$ edge of $Sr_2CuO_2Cl_2$. Open and closed symbols stem from 2 independent measurements on different samples. In the [100] direction, data for both $q_x > 0$ and $q_x < 0$ are collapsed on the same $(0, 0) - (\pi, 0)$ branch. The dot-dashed line is the LSWT result (including the Oguchi correction [104]) for a nearest neighbor Heisenberg model with $J = 130$ meV. The black dashed line is a nearest-neighbor Hubbard model fit for $t = 0.261 \pm 0.004$ eV and $U = 1.59 \pm 0.04$ eV. For the gray lines, further neighbor hoppings are added to the Hubbard model. Reasonable fits can also be obtained at larger $U$: the thickness of the gray band is generated by taking 1.9 eV $< U <$ 4 eV, while fitting the hopping parameters. Guarise *et al.* [69] experimentally establish a relation between $U$ and the hopping parameters. All measurements were done at $T = 15$ K. Figure from Ref. [69]

RIXS experiments have not only mapped out the magnon dispersion, they have also verified the predicted spectral weight of the magnon peak in various cuprates. Since the experimental spectral weight is sensitive to, amongst others, self-absorption, Braicovich *et al.* [21] compared the ratio of spectral weights for $\sigma$ and $\pi$ polarization while keeping the incident and outgoing photon directions constant – thus reducing the effect of self-absorption. The data and theory are first normalized to the spectral weight of the dd excitations, which are well-understood theoretically [19, 20]. Then, the single magnon spectral weight for $\sigma$ polarization is divided by the signal for $\pi$ polarization. One finds that the resulting linear dichroism ratio $R$ of the (renormalized) theoretical intensities is

$$R = \frac{I_\sigma}{I_\pi} = \frac{\sum_{\boldsymbol{\epsilon}'} \left| T_{\mathrm{sf}}(\boldsymbol{\epsilon}', \boldsymbol{\epsilon}_\sigma) \right|^2}{\sum_{\boldsymbol{\epsilon}'} \left| T_{\mathrm{sf}}(\boldsymbol{\epsilon}', \boldsymbol{\epsilon}_\pi) \right|^2}, \tag{4.71}$$

*i.e.*, independent of the dynamic, $\mathbf{q}$ dependent spin susceptibilities. Only the local, atomic spin flip scattering factors $T_{\mathrm{sf}}$ remain in the ratio. Fig. 4.15 shows the linear dichroism ratio, which has a clear asymmetry between $+\mathbf{q}$ and $-\mathbf{q}$. The agreement between theory and experiments is again very good.

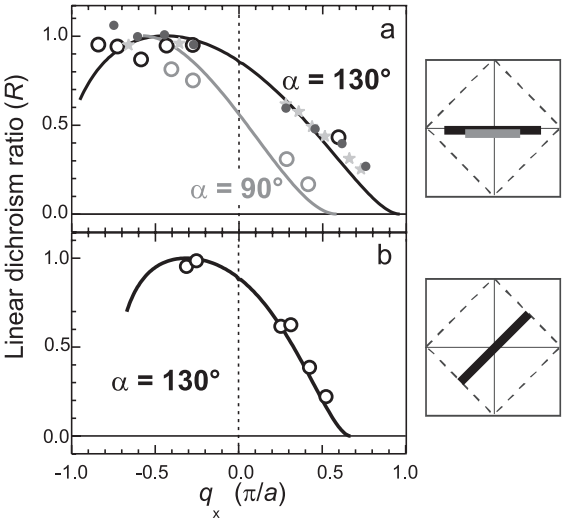


**Figure 4.15:** Single magnon spectral weight measured at the copper $L_3$ edge of various cuprates with transferred momentum along (a) the [100] direction, and (b) the [110] direction. The open circles refer to $La_2CuO_4$, the filled circles to (Sr,Ca)$CuO_2$ (prepared as a thin film on $SrTiO_3$), and the stars to strongly underdoped $NdBa_2Cu_3O_{6+\delta}$. The data were taken at $T = 15$ K. $\alpha$ is the scattering angle. Figures from Ref. [21].

### 4.5.3 Bimagnon excitations at the Cu L edge

Published in '*Dispersion of Magnetic Excitations in the Cuprate $La_2CuO_4$ and $CaCuO_2$ Compounds Measured Using Resonant X-Ray Scattering*', Phys. Rev. Lett. **102**, 167401 (2009) with L. Braicovich, V. Bisogni, F. Forte, C. Aruta, G. Balestrino, N. B. Brookes, G. M. De Luca, P. G. Medaglia, F. Miletto Granozio, M. Radovic, M. Salluzzo, J. van den Brink, and G. Ghiringhelli.

Next to single magnons, the Cu L edge can also exhibit bimagnon excitations [10]. Single magnons will dominate the RIXS spectrum as they arise in direct RIXS processes, but at the high energy side of the single magnon peak, a tail is observed [11]. This could well be multi-magnon excitations.

Bimagnon excitations arise in RIXS at the Cu L edge because the $3d^{10}$ configuration in the intermediate state blocks all superexchange. The spins of its neighbors reorient themselves, and this process can be described in terms of bimagnon excitations. The blocking of superexchange bonds is formalized in the intermediate state Hamiltonian

$$\bar{H} = H_0 - J \sum_{i,\delta} p_i p_i^\dagger \mathbf{S}_i \cdot \mathbf{S}_{i+\delta}, \tag{4.72}$$

where $p_i$ annihilates a 2p core electron at site $i$ and $\delta$ points to nearest neighbors. To first order in the UCL expansion, we find

$$\mathcal{F}_{fi} = \frac{T_{\rm el}(\boldsymbol{\epsilon}', \boldsymbol{\epsilon})}{(i\Gamma)^2} \langle f | \sum_i e^{i\mathbf{q}\cdot\mathbf{R}_i} p_i^\dagger \bar{H} p_i \, | i \rangle \tag{4.73}$$

where the polarization dependence is the same as for elastic scattering as the Hamiltonian should excite the valence electrons in indirect RIXS. Of course, the dipole transitions can also add other excitations like dd or spin flip excitations, but we are not interested in these processes here. As Eqs. (4.72) and (4.36) have the same form, the Cu L edge bimagnon spectra have the same line shape as the bimagnon spectra at the Cu K edge [see Fig. 4.5(a)], and we therefore will not elaborate on this subject here.

### 4.5.4 Chemical pressure effects

Published as '*Effect of the chemical pressure on bimagnons in antiferromagnetic insulators: $CaCuO_2$ and $BaCuO_2$ studied with Cu-$L_3$ resonant inelastic X-ray scattering*' in Eur. Phys. J. Special Topics **169**, 141 (2009) with V. Bisogni, C. Aruta, G. Balestrino, N. B. Brookes, F. Forte, G. Ghiringhelli, P. G. Medaglia, J. van den Brink, and L. Braicovich.

When the lattice parameter of a magnetic solid is changed, the hopping amplitudes change too, and ultimately also the superexchange constant is altered. A comparison of $CaCuO_2$ with $BaCuO_2$ with Cu $L_3$ edge RIXS is presented by Bisogni *et al.* [118]. Ba is a bigger ion than Ca and therefore increases the lattice parameters by a factor of 1.03 in-plane, and 1.27 along the $z$ axis, making the crystal field in $BaCuO_2$ more cubic. The increase in the in-plane lattice parameters reduces the superexchange constant. An energy shift is observed for the magnetic spectrum, implying that $J$ is reduced by a factor of $0.67 \pm 0.06$ when substituting Ca by Ba.

For the dd excitations, the (average) observed scaling factor for the energy is different: $0.8 \pm 0.06$. This should be ascribed to the more cubic symmetry of the crystal field, which rearranges the energies of the different dd excitations.

Further, a reduction in the spectral weight of the low energy spectrum is seen of at least a factor 0.5 when the data is normalized to the total dd excitations' spectral weight. In interpreting this fact, one has to take into account that the large increase of the lattice parameter in the $z$ direction changes the radial matrix elements. The radial parts of all the wave functions become more similar in the more cubic Ba compound, while in $CaCuO_2$, the radial parts differ substantially for the different 3d orbtals because of the $D_{4h}$ crystal field splitting.

### 4.5.5 Spectral weight at the Γ point

Both the single magnon and the bimagnon spectral weight vanish at $\mathbf{q} = \mathbf{0}$. The question then arises which higher order process gives spectral weight at the Γ point. The single magnon DOS vanishes at $\mathbf{q} = \mathbf{0}$, so unless there is some mixing with other wave vectors, there cannot be any single magnon spectral weight at the Γ point. The bimagnon DOS, however, is very large at $\mathbf{q} = \mathbf{0}$ [see Fig. 4.5(b)]. In Sec. 4.4, we discussed bimagnon excitations that arise in the second order of

the UCL expansion, generating spectral weight at $\mathbf{q} = \mathbf{0}$, proportional to $(J/\Gamma)^4$. This also holds at the Cu L edge, of course. Here, we consider another possible mechanism: multi-site exchange mechanisms that are not included in the simple Heisenberg model also give rise to bimagnon excitations, in particular at the $\Gamma$ point.

Starting from a single-band Hubbard model, multi-site exchange processes appear in the effective spin Hamiltonian at fourth order in $t/U$. Such processes contribute to the scattering amplitude in two ways: first, the initial and final states are modified. Second, the intermediate state energies are modified, and in the UCL expansion, this is reflected in a modified $\bar{H}$.

The Heisenberg Hamiltonian to fourth order in $t/U$ without a core hole is given by Eq. (4.14). The corresponding magnon (approximate) eigenstates that determine the initial and final states are given in Sec. 4.2.

The fourth order contribution to the intermediate state Hamiltonian (*i.e.*, including the core hole) is obtained through a tedious calculation using degenerate perturbation theory of the Hubbard model to fourth order [82,119]. The Hubbard Hamiltonian of the system with a core hole is written as $\bar{H} = h + V$ where $h$ contains the Coulomb repulsion part (including the 2p-3d Coulomb energy $U_c$) and $V$ contains the hopping. Turning off the hopping, the (degenerate) ground state has the core hole site doubly occupied and all other sites singly occupied. The projector on the space spanned by all these ground states is $P_0$. Turning on a small hopping parameter $t$ introduces exchange interactions. The effective Hamiltonian to fourth order in $t/U$ is [82, 119]:

$$\begin{aligned}\bar{H}^{(4)}_{\text{eff}} = {} & P_0VSVP_0 + P_0VSVSVSVP_0 \\ & - \frac{1}{2}\left(P_0VS^2VP_0VSVP_0 + P_0VSVP_0VS^2VP_0\right) \end{aligned} \tag{4.74}$$

where $S = (P_0 - \mathbb{1})/h$. Because of the projectors $P_0$, the eigenstates of the effective Hamiltonian are also eigenstates of $P_0$ and can be reformulated in terms of spins, see Eq. (2.14) of Ref. [82]. The first term on the right-hand side of Eq. (4.74) generates the familiar nearest neighbor exchange (which is blocked at the core hole site, however). The other terms in Eq. (4.74) involve four hops, which after two hops may [terms between parentheses in Eq. (4.74)] or may not [$P_0VSVSVSVP_0$] return to the space of unperturbed ground states.

The details of the derivation of the low energy effective Hamiltonian $\bar{H}_{\text{eff}}$ to $4^{\text{th}}$ order in $t/U_{(c)}$ can be found in appendix D. The resulting intermediate state Hamiltonian in the mean field approximation is

$$\begin{aligned}\bar{H}^{(4)}_{\text{eff}} = H_0 + \sum_i p_i p_i^\dagger \Bigg[ & \sum_j^{\text{nn}} \left(\frac{64t^4}{U^3} - \frac{4t^2}{U}\right) \mathbf{S}_i \cdot \mathbf{S}_j + \sum_j^{\text{nnn}} \frac{20t^4}{U^3} \mathbf{S}_i \cdot \mathbf{S}_j \\ & + \sum_{j \neq k} \left(\frac{4t^4}{UU_c^2} + \frac{8t^4}{U_c^2(2U_c + U)} - \frac{4t^4}{U^3}\right) \mathbf{S}_j \cdot \mathbf{S}_k +\end{aligned}$$

$$+\sum_{\text{squares}}\left\{\left(\frac{24t^4}{U^3}-\frac{2t^4}{U_c^3}-\frac{2t^4}{UU_c^2}\right)(\mathbf{S}_j\cdot\mathbf{S}_k+\mathbf{S}_k\cdot\mathbf{S}_l)\right.$$
$$\left.+\left(\frac{20t^4}{U^3}-\frac{2t^4}{U_c^3}-\frac{2t^4}{UU_c^2}\right)\mathbf{S}_j\cdot\mathbf{S}_l\right\}\Bigg]. \tag{4.75}$$

The sums between the straight brackets are, respectively, over all nearest neighbors (nn) $j$ of $i$, over all next nearest neighbors (nnn) $j$ of $i$, over all pairs $j,k$ of nearest neighbors of $i$, and over all squares of $2\times 2$ sites containing $i$.

Eq. (4.75) is substituted in the UCL expansion. The leading inelastic order is

$$\mathcal{F}_{fi}=\frac{1}{(i\Gamma)^2}\langle f|\,\mathcal{D}^\dagger\bar{H}^{(4)}_{\text{eff}}\mathcal{D}\,|i\rangle=-\frac{T_{\text{el}}(\boldsymbol{\epsilon}',\boldsymbol{\epsilon})}{\Gamma^2}\langle f|\sum_i e^{i\mathbf{q}\cdot\mathbf{R}_i}[\dots]\,|i\rangle\,, \tag{4.76}$$

where $[\dots]$ represents the lengthy expression between striaght brackets in Eq. (4.75). The polarization factor for elastic scattering is the same as in Eq. (4.73).

In appendix D.2, the scattering amplitude for two-magnon creation processes at zero temperature is evaluated. The result is

$$\begin{aligned}\mathcal{F}_{fi}=&-\frac{T_{\text{el}}(\boldsymbol{\epsilon}',\boldsymbol{\epsilon})}{\Gamma^2}\sum_{\mathbf{k}}\Bigg[\Bigg\{-\left(\frac{20t^4}{U^3}-\frac{2t^4}{U_c^3}-\frac{2t^4}{UU_c^2}\right)f_b(\mathbf{k},\mathbf{q})-\frac{20t^4}{U^3}f_{\text{nnn}}(\mathbf{k},\mathbf{q})\\
&-\left(\frac{4t^4}{UU_c^2}+\frac{8t^4}{U_c^2(2U_c+U)}-\frac{4t^4}{U^3}\right)f_a(\mathbf{k},\mathbf{q})-\left(\frac{64t^4}{U^3}-\frac{4t^2}{U}\right)(1+\gamma_{\mathbf{q}})\\
&-\left(\frac{24t^4}{U^3}-\frac{2t^4}{U_c^3}-\frac{2t^4}{UU_c^2}\right)f_{c1}(\mathbf{q})\Bigg\}(U_{\mathbf{k}}V_{\mathbf{k}-\mathbf{q}}+U_{\mathbf{k}-\mathbf{q}}V_{\mathbf{k}})\\
&+\left\{\left(\frac{64t^4}{U^3}-\frac{4t^2}{U}\right)(\gamma_{\mathbf{k}-\mathbf{q}}+\gamma_{\mathbf{k}})+\left(\frac{24t^4}{U^3}-\frac{2t^4}{U_c^3}-\frac{2t^4}{UU_c^2}\right)f_{c2}(\mathbf{k},\mathbf{q})\right\}\\
&\times(U_{\mathbf{k}}U_{\mathbf{k}-\mathbf{q}}+V_{\mathbf{k}-\mathbf{q}}V_{\mathbf{k}})\Bigg]\langle f|\,\alpha^\dagger_{\mathbf{k}}\alpha^\dagger_{-\mathbf{k}+\mathbf{q}}\,|0\rangle\,.\end{aligned} \tag{4.77}$$

At $\mathbf{q}=\mathbf{0}$, the amplitude reduces to

$$\begin{aligned}\mathcal{F}_{fi}=&\frac{T_{\text{el}}(\boldsymbol{\epsilon}',\boldsymbol{\epsilon})}{\Gamma^2}\sum_{\mathbf{k}}\Bigg[\Bigg\{\left(\frac{4t^4}{UU_c^2}+\frac{8t^4}{U_c^2(2U_c+U)}-\frac{4t^4}{U^3}\right)f_a(\mathbf{k},\mathbf{0})\\
&\left(\frac{30t^4}{U^3}-\frac{2t^4}{U_c^3}-\frac{2t^4}{UU_c^2}\right)f_b(\mathbf{k},\mathbf{0})\Bigg\}2U_{\mathbf{k}}V_{\mathbf{k}}\Bigg]\langle f|\,\alpha^\dagger_{\mathbf{k}}\alpha^\dagger_{-\mathbf{k}}\,|0\rangle\end{aligned} \tag{4.78}$$

with

$$f_a(\mathbf{k},\mathbf{0})=2\gamma_{2\mathbf{k}}-2+f_b(\mathbf{k},\mathbf{0}),\qquad f_b(\mathbf{k},\mathbf{0})=4\cos k_x\cos k_y-4. \tag{4.79}$$

Using the parameters (obtained by neutron scattering on $La_2CuO_4$) $t = 0.33$ eV, $U = 2.9$ eV [83], and $U_c = 4.1$ eV [61], one finds

$$\frac{4t^4}{UU_c^2} + \frac{8t^4}{U_c^2(2U_c+U)} - \frac{4t^4}{U^3} \approx -0.4 \text{ meV}, \tag{4.80}$$

$$\frac{30t^4}{U^3} - \frac{2t^4}{U_c^3} - \frac{2t^4}{UU_c^2} \approx 13.7 \text{ meV}. \tag{4.81}$$

We now make a rough comparison between the spectral weight coming from corrections to the Hamiltonian, and from the second order of the UCL expansion. In Sec. 4.4, it is shown that the second order of the UCL expansion (4.62) gives the following contribution at $\mathbf{q} = \mathbf{0}$:

$$\mathcal{F}_{2^{\text{nd}}UCL} = \frac{T_{\text{el}}(\boldsymbol{\epsilon}', \boldsymbol{\epsilon})}{\Gamma^2} \frac{J^2}{4i\Gamma} \sum_{\mathbf{k}} \langle f |\, f_a(\mathbf{k}, \mathbf{0}) 2U_{\mathbf{k}} V_{\mathbf{k}}\, \alpha^\dagger_{\mathbf{k}} \alpha^\dagger_{-\mathbf{k}} \,|0\rangle \,. \tag{4.82}$$

Ignoring all details in the functions $f$, we compare $13.7 - 0.4 = 13.3$ meV for the higher order exchange scenario with $J^2/2\Gamma \approx 15.6$ meV for the second order of the UCL expansion at the Cu $L_3$ edge. We conclude that both the second order of the UCL expansion and higher order exchange processes contribute significantly to the Cu $L_3$ RIXS intensity at the $\Gamma$ point. It should be noted that the higher order exchange processes dominate the $\mathbf{q} = \mathbf{0}$ RIXS intensity when $\Gamma$ is larger, as, *e.g.*, at the $L_2$ and K edges.

## 4.6 Copper L edge of doped cuprates

Now that the magnetic RIXS spectrum of the undoped cuprates is understood to a fair level of detail, the next question to be addressed is the following: how does the low energy $L_3$ edge RIXS spectrum evolve upon doping?

The X-ray absorption spectrum of undoped $La_2CuO_4$ at the Cu $L_3$ edge shows a single peak, corresponding (mainly) to the transition $3d^9 \rightarrow \underline{2p}_{3/2}3d^{10}$. When $La_2CuO_4$ is doped with holes, this peak aquires a tail at the high energy side, which is interpreted as $3d^9\underline{L} \rightarrow \underline{2p}_{3/2}3d^{10}\underline{L}$ [84]. The energy is slightly higher because one breaks up a Zhang Rice Singlet (ZRS) in the latter process, which costs some energy. From the XAS spectra, it therefore seems possible to tune X-ray photons so that they are absorbed either at the undoped or at the doped sites of $La_{2-x}Sr_xCuO_4$. These resonances are called the $L_3$ and $L_3'$ edges, respectively.

We assume that the low energy physics of doped cuprates are described by the t-J model. Of course, phonons will also play a role, but the treatment of phonon excitations in RIXS is postponed to chapter 7. The Hamiltonian for the t-J model reads

$$H_0 = H_t + H_J = -t \sum_{\langle i,j\rangle,\sigma} \left( d^\dagger_{i\sigma} d_{j\sigma} + \text{h.c.} \right) + J \sum_{\langle i,j\rangle} \mathbf{S}_i \cdot \mathbf{S}_j. \tag{4.83}$$

The $d_{i\sigma}^{(\dagger)}$ operators annihilate (create) an electron on site $i$ with spin $\sigma$, and the sums over $\langle i,j\rangle$ count each bond once. Unoccupied sites correspond to ZRS's.

### 4.6.1 RIXS amplitude for doped cuprates

We now consider the RIXS amplitude when the X-ray photons are tuned to the $L_3$ edge. As mentioned above, we assume that only sites that do not carry ZRS's are excited. This can be incorporated in the Kramers-Heisenberg equation by projecting out all intermediate states that have a ZRS at the core hole site. We write Eq. 2.41 as

$$\mathcal{F}_{fi} = \sum_{\zeta\in\{\text{el,sf}\}} T_\zeta(\boldsymbol{\epsilon}',\boldsymbol{\epsilon}) \sum_i e^{i\mathbf{q}\cdot\mathbf{R}_i} \sum_n \frac{\langle f|\, d_{i\sigma'} p_{i\sigma'}^\dagger P\,|n\rangle\,\langle n|\, P\, p_{i\sigma} d_{i\sigma}^\dagger\,|i\rangle}{z - E_n} \tag{4.84}$$

where $\zeta$ indicates either a spin flip process or an elastic scattering event, and determines the spins $\sigma$ and $\sigma'$. Further, $z = E_g + \hbar\omega_{\mathbf{k}} + i\Gamma$, $p_{i\sigma}$ is the 2p core electron annihilation operator and $P$ the projection operator

$$P = \sum_{i,\sigma} p_{i\sigma} p_{i\sigma}^\dagger n_{i\uparrow} n_{i\downarrow}, \tag{4.85}$$

removing any contribution to the amplitude coming from X-ray transitions at ZRS sites. Note that $n_{i\sigma} = d_{i\sigma}^\dagger d_{i\sigma}$. We assume that the RIXS process remains a predominantly local one, *i.e.*, a local $3d^{10}$ intermediate state is created, so the polarization factors $T_\zeta$ are the same as for the undoped cuprates: at low energy loss, they either yield a spin flip or an elastic process.

At the Cu $L_3$ edge of the undoped compounds, the main source of low energy inelastic spectral weight is spin flip scattering. In doped cuprates, it is also possible to rearrange the charges. As will be shown below, charge scattering happens even when the intermediate state dynamics are absent, and springs from the elastic scattering channel when the Cu ions are interacting with each other. This is analogous to the spin flip cross section for single ions, which also depends strongly on the way the electrons of the system interact. We ignore the dd excitations here, because they do not affect the low energy spectra. The question now arises which channel dominates the low energy RIXS spectra of doped cuprates: magnetic or charge scattering?

### 4.6.2 Fast collision approximation

To answer the question which scattering channel dominates the low energy RIXS spectra of the cuprates, we first make the fast collision approximation, *i.e.*, keeping only the zeroth order of the UCL expansion.In the undoped case, the single magnon spectrum is quite accurately described by the fast collision approximation (4.68). When the system is doped and the incident energy is tuned to the

sites with a spin, the sum over sites should exclude all hole sites. This is enforced in Eq. (4.84) by the projection operator $P$. The spin flip scattering amplitude is

$$\mathcal{F}_{fi}^{\mathrm{sf}} = \frac{T_{\mathrm{sf}}(\boldsymbol{\epsilon}', \boldsymbol{\epsilon})}{i\Gamma} \langle f| \sum_i e^{i\mathbf{q}\cdot\mathbf{R}_i} \sigma_i^z \rho_i) \, |i\rangle + \mathcal{O}(\Gamma^{-2}) \tag{4.86}$$

where we introduced the density operator $\rho_i = n_{\uparrow i} + n_{\downarrow i}$.

Calculating this correlation function within the t-J model is, of course, difficult. Compared to the undoped compounds, we expect spectral weight to leak to higher energies because of the new, higher energy scale introduced by hopping. Also, the magnon peak is expected to significantly broaden and lose weight (it loses coherence), analogous to the evolution of the two-magnon Raman spectra with doping [120]. To see how much spectral weight is in the spin flip cross section, we integrate it over energy loss and transferred momentum, and get

$$\begin{aligned}
\frac{1}{N} \sum_{\mathbf{q}} \int d\omega \frac{d^2\sigma}{d\Omega d\omega} &= \frac{|T_{\mathrm{sf}}(\boldsymbol{\epsilon}', \boldsymbol{\epsilon})|^2}{\Gamma^2} \langle i| \sum_{\mathbf{q},i,j} \frac{e^{-i\mathbf{q}\cdot\mathbf{R}_j}}{N} \rho_j \sigma_j^z e^{i\mathbf{q}\cdot\mathbf{R}_i} \sigma_i^z \rho_i \, |i\rangle \\
&= \frac{|T_{\mathrm{sf}}(\boldsymbol{\epsilon}', \boldsymbol{\epsilon})|^2}{\Gamma^2} \langle i| \sum_i \rho_i (\sigma_i^z)^2 \rho_i \, |i\rangle \\
&= \frac{|T_{\mathrm{sf}}(\boldsymbol{\epsilon}', \boldsymbol{\epsilon})|^2}{\Gamma^2} \langle i| \sum_i \rho_i \, |i\rangle = \frac{|T_{\mathrm{sf}}(\boldsymbol{\epsilon}', \boldsymbol{\epsilon})|^2}{\Gamma^2} N(1-x).
\end{aligned} \tag{4.87}$$

We conclude that the total spin flip intensity scales linearly with doping. This result is valid for all doping $x$.

Next to spin flip scattering, there is also the elastic scattering channel. Note that we mean with 'elastic scattering channel' that $\nu = \nu'$ in Eq. (2.42), and emphatically not that $\omega = 0$. In an ideal crystal, all intensity is pushed to the Bragg conditions $\mathbf{G}$. Upon doping, the elastic scattering channel at the $L_3$ edge in the fast collision approximation becomes

$$\mathcal{F}_{fi}^{\mathrm{el}} = \frac{T_{\mathrm{el}}(\boldsymbol{\epsilon}', \boldsymbol{\epsilon})}{i\Gamma} \langle f| \sum_i e^{i\mathbf{q}\cdot\mathbf{R}_i} \rho_i \, |i\rangle + \mathcal{O}(\Gamma^{-2}), \tag{4.88}$$

with $T_{\mathrm{el}}(\boldsymbol{\epsilon}', \boldsymbol{\epsilon})$ the atomic scattering factor for the elastic channel. The elastic channel thus gives rise to charge scattering.

It might appear strange that one arrives at charge scattering through the elastic scattering channel. In the case of non-interacting ions, there is no inelastic scattering: the above expression gives spectral weight at $\omega = 0$ only. The elastic peak is expected to gain intensity away from Bragg conditions upon doping as the holes constitute impurities in the crystal from the photon's perspective. When the ions interact, the holes are allowed to move, and hole and spin sites mix.

As with the magnetic cross section, it is complicated to evaluate the exact correlation function for charge scattering in the t-J model. The total spectral

weight of the elastic channel for the hole-doped cuprates is

$$\frac{1}{N}\sum_{\mathbf{q}}\int d\omega \frac{d^2\sigma}{d\Omega d\omega} = \frac{\left|T_{\rm el}(\boldsymbol{\epsilon}',\boldsymbol{\epsilon})\right|^2}{\Gamma^2 N}\sum_{\mathbf{q}}\langle i|\,\rho_{-\mathbf{q}}\rho_{\mathbf{q}}\,|i\rangle + \mathcal{O}(\Gamma^{-3})$$
$$= \frac{\left|T_{\rm el}(\boldsymbol{\epsilon}',\boldsymbol{\epsilon})\right|^2}{\Gamma^2}\langle i|\sum_{i,j}\delta_{i,j}\rho_i\rho_j\,|i\rangle = \frac{\left|T_{\rm el}(\boldsymbol{\epsilon}',\boldsymbol{\epsilon})\right|^2}{\Gamma^2}N(1-x). \qquad (4.89)$$

The elastic channel is reduced as $1-x$, as expected for a decreasing number of scattering centers. It can be easily checked that the intensity of the Bragg peak reduces as $1-2x$, and it follows that the elastic scattering channel gives rise to inelastic charge scattering with intensity proportional to $x$.

The evaluation of the charge scattering operator is a difficult task, and the center of much effort. In the special case of very low doping, the holes in hole-doped cuprates reside around $(\pi/2,\pi/2)$, according to ARPES data. In RIXS, these holes are scattered to approximately $(\pi/2,\pi/2)+\mathbf{q}$. There are $xN$ holes around $(\pi/2,\pi/2)$ in the initial state, so we approximate the charge intensity as

$$\left.\frac{d^2\sigma}{d\Omega d\omega}\right|_{\rm charge} \approx \frac{T_{\rm el}(\boldsymbol{\epsilon}',\boldsymbol{\epsilon})^2 xN}{\Gamma^2}\delta(\omega-\epsilon_{\mathbf{q}+(\pi/2,\pi/2)}) \qquad (4.90)$$

where $\epsilon_{\mathbf{q}}$ is the 'energy' of a hole with momentum $\mathbf{q}$. This is of course a sloppy approach: the holes are heavily dressed by, for instance, phonons, see Shen *et al.* [121]. Therefore, the hole dispersion relation is fuzzy and not a delta function[3]. The dispersion of quasiparticles in several strongly underdoped compounds is given in, for instance, Ref. [122–125]. For higher dopings (up to the overdoped, Fermi liquid phase of the t-J model), the dynamic charge and spin correlation functions are calculated in, *e.g.*, Refs. [126–129].

Although the exact magnetic and charge spectra are hard to predict, we have shown above that charge scattering scales linearly with doping, and is proportional to the elastic atomic scattering factor. Similarly, the magnetic RIXS intensity decreases linearly with doping, and stays proportional to $T_{\rm sf}(\boldsymbol{\epsilon}',\boldsymbol{\epsilon})$. Since the dynamic spin and charge correlation functions are symmetric under inversion of space, any asymmetry between spectra at $+\mathbf{q}$ and $-\mathbf{q}$ is generated by the atomic scattering factors. In particular, for $\mathbf{q}$ along the $(\pi,0)$ direction, $T_{\rm el}$ is also symmetric under inversion [19], and any asymmetry seen in such spectra arises through to the magnetic scattering channel. Further, in the special case of $\mathbf{q}=(0,0)$, it can be seen from Eqs. (4.86) and (4.88) that the inelastic magnetic and charge signals are zero. In the case of magnetic scattering, the scattering operator is proportional to the total spin along the $z$ axis, which is a constant. In the case of charge scattering, the scattering operator counts the total charge,

[3]Note that we do not remove electrons as in ARPES. The number of holes is conserved in RIXS, and in the charge-neutral final state the coupling to phonons might be reduced compared to ARPES.

which also is a constant. In the limit of very low doping, we found that the RIXS charge cross section traces the hole dispersion.

### 4.6.3 Experimental data

Although it is difficult to make a detailed comparison between theory and experiment because of the complicated correlation functions in the theory, recent RIXS experiments on 8.5% doped $La_{2-x}Sr_xCuO_4$ [11] can put the theory to some tests.

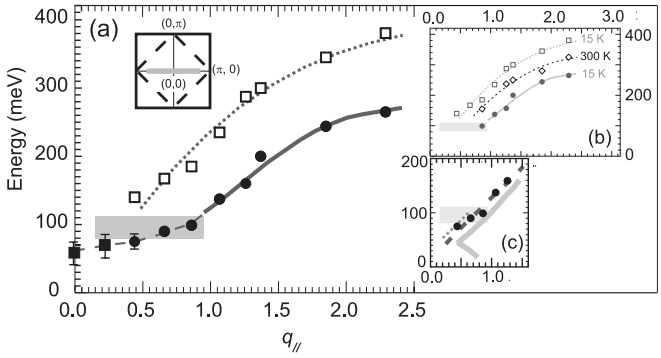


**Figure 4.16:** RIXS data on 8.5% doped $La_{2-x}Sr_xCuO_4$ at $T = 15$ K, *i.e.*, in the superconducting state, with transferred momentum along the $(\pi, 0)$ direction, show (a) two dispersing branches that (b) merge into a single branch at room temperature. At low energy loss, the two features are hard to resolve because of phonons. In Fig. (a), the dotted line is the magnon dispersion from the undoped compound, multiplied by 1.09. The solid line is a guide to the eye. (c) Comparison to inelastic neutron scattering data taken around $\mathbf{q} = (\pi, \pi)$ (dotted line: $x = 0.05$, dashed line: $x = 0.085$, thick line: $x = 0.16$). Note that the RIXS data is taken around the center of the Brillouin zone, and that these regions are not necessarily equivalent in a doped compound where the long range magnetic order is absent. Figure from Braicovich *et al.* [11].

First, our theory predicts that both the elastic and magnetic scattering channels give no spectral weight at the Γ point. This agrees quite well with the RIXS data of Ref. [11], which mainly shows an elastic line at $\mathbf{q} = \mathbf{0}$.

Second, at low doping, the magnetic spectral weight is reduced by only $x = 8.5\%$ relative to the undoped compound. Since the RIXS spectra of the undoped compound are magnetic in nature (there is no charge contribution there), we expect the spectra of the doped compounds to be dominated by magnetic scattering as well. Indeed, the low energy spectra from Ref. [11] are very different for $+\mathbf{q}$ and $-\mathbf{q}$, implying that the spectra are dominated by magnetic scattering, as explained above.

In the data, two dispersing branches are seen, whose dispersions are shown

in Fig. 4.16. (Both are ascribed to the magnetic channel.) The lower branch is also observed with neutron scattering, the higher one not. That could be due to experimental limitations of neutron scattering. The higher branch coincides with the magnon dispersion if the latter is rescaled by a factor 1.09. However, in Raman scattering data, the two-magnon excitation is seen to go down in energy upon doping: in Fig. 9(b) of Ref. [120], the two-magnon signal moves from 3300 $\mathrm{cm}^{-1}$ in $La_2CuO_4$ to 2700 $\mathrm{cm}^{-1}$ in the 8% doped compound.

## 4.7 Oxygen K edge

The oxygen K edge (1s $\rightarrow$ 2p) is a peculiar edge since it is in principle direct RIXS (the core electron is excited into the 2p valence bands), but the core level spin-orbit coupling is absent. Single spin flips are therefore forbidden at the O K edge, and low energy excitations can only occur via the indirect channel. Two-magnon excitations are allowed and give a strong, non-dispersive signal at high energy loss, even for small $\mathbf{q}$, as will be shown in Sec. 4.7.2.

The O K edge is a difficult edge for experiments, since in the cuprates the O ions have a filled 2p subshell. Only through hybridization with the Cu hole is it possible to excite a core electron. Usually, the Cu hole is in the $3d_{x^2-y^2}$ orbital and this orbital hybridizes with the O 2p orbitals that are directed towards the lobes of the $x^2$-$y^2$ wave function: $2p_x$ along the $x$ direction and $2p_y$ along the $y$ direction. The wave function of the valence hole is therefore

$$|\psi\rangle = \cos\theta \left|3d^9\right\rangle + \sin\theta \left|3d^{10}\underline{\mathrm{L}}\right\rangle \tag{4.91}$$

where both states have $x^2 - y^2$ symmetry and $\theta$ is a small number parametrizing the hybridization. $\underline{\mathrm{L}}$ means that the hole is on the oxygen ions. The dipole matrix element $\langle\psi|\,\mathcal{D}\,|O\ 1s\rangle$ is small: it is controlled by $\sin\theta$ and the smallness of the overlap of O 1s with Cu 3d orbitals. The result is that O K edge experiments suffer from low intensity. Most of the radiative decay processes will be via the fluorescence channels, where the hole in the final state is on an O ion.

Notwithstanding this difficulty, RIXS experiments at the O K edge of $La_2CuO_4$ have been successfully performed [70]. The low energy region shows spectral weight ranging from 0 to 1 eV, peaking at 0.5 eV and dispersing very little.

In this section, we discuss the magnetic excitations to be expected at the O K edge. The polarization dependence is strikingly different from the Cu edges, and will be explained in Sec. 4.7.1. Then, the expected magnetic RIXS signal will be presented in detail in Sec. 4.7.2 and compared to the present data [70]. Finally, we will consider other possible contributions to the low energy RIXS spectrum in Sec. 4.7.3.

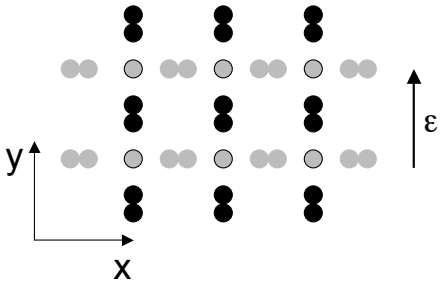


**Figure 4.17:** Polarization dependence of the absorption of X-rays at the O K edge. The oxygen ions with the black 2p orbitals can be excited with RIXS when the polarization is directed along the $y$ axis, while the gray oxygen ions are then inactive. The gray circles with black borders represent the Cu ions.

### 4.7.1 Polarization dependence

It is assumed that only the $2p_{x,y}$ orbitals of the in-plane O ions hybridize with the Cu levels. The 2p orbitals of the out-of-plane O ions do not hybridize because of the $x^2$-$y^2$ symmetry of the hole wave function. Therefore, the out-of-plane O ions are assumed not to be active in O K edge RIXS. In that case, one finds a remarkable polarization dependence: when the polarization vector of the incoming photon is aligned along the $x$ axis, only the O ions that connect Cu ions along the $x$ direction are excited. When the polarization vector is aligned along the $y$ direction, only those O ions are excited that connect Cu ions along the $y$ direction, see Fig. 4.17. This can be easily seen by writing the dipole matrix elements as

$$\langle O\ 2p_{x_j} | \mathcal{D} | O\ 1s \rangle \propto \int d\mathbf{r}\ x_j x_i \epsilon_i \propto \epsilon_j. \tag{4.92}$$

The full dipole operator is

$$\begin{aligned} \mathcal{D} \propto \langle 3d^{10} | \mathbf{D} | \psi \rangle \cdot \boldsymbol{\epsilon} \propto \sum_i e^{i\mathbf{k}\cdot\mathbf{R}_i} \sin\theta \langle 2p_x | x | 1s \rangle \\ \times \left[ \epsilon_x (e^{-i\mathbf{k}\cdot\hat{\mathbf{x}}} s_{i-\hat{\mathbf{x}}} - e^{i\mathbf{k}\cdot\hat{\mathbf{x}}} s_{i+\hat{\mathbf{x}}}) + \epsilon_y (e^{i\mathbf{k}\cdot\hat{\mathbf{y}}} s_{i+\hat{\mathbf{y}}} - e^{-i\mathbf{k}\cdot\hat{\mathbf{y}}} s_{i-\hat{\mathbf{y}}}) \right], \end{aligned} \tag{4.93}$$

where $3d^{10}$ represents the Cu $3d^{10}$, O $2p^6$ intermediate state. The minus signs in front of the 1s core electron annihilation operators $s_i$ come from the way the 2p orbitals are hybridized with the Cu $x^2$-$y^2$ orbital. The creation operators for the 2p electrons are suppressed. The vectors $\hat{\mathbf{x}}, \hat{\mathbf{y}}$ point from the central Cu ion at position $\mathbf{R}_i$ to the neighboring in-plane oxygen ions. The dipole matrix element of the O 1s core orbital with the Cu $3d_{x^2-y^2}$ orbital is neglected here, but give approximately the same polarization dependence.

The above polarization dependence introduces an anisotropy in the scattering amplitude. Magnetic scattering is therefore expected to be different from the Cu edges, where the modification of the superexchange bonds is isotropic. Now, only bonds along either the $x$ or the $y$ direction are modified. If the polarization vector is directed along the [110] direction, all oxygens are active, but because of the photon phase factors, we do not expect to recover the Cu results.

### 4.7.2 Two-magnon contribution to the RIXS spectrum

Since the direct RIXS channel is absent in oxygen, we calculate the indirect magnetic RIXS spectrum to first order in the UCL expansion. The result is a two-magnon spectrum, like at the Cu K edge, but with different RIXS matrix elements because of the different excitation processes. As can be seen in Fig. 4.5(b), most of the two-magnon states have energies around $4J$ (neglecting renormalizations due to magnon-magnon interactions). The large dispersion of the two-magnon spectrum at the Cu edges is therefore a peculiar matrix element effect. Since at the O K edge, the matrix elements are different, one would in general not expect that this peculiar effect survives. The O K edge RIXS signal would likely be more like the two-magnon DOS: peaked at high energy loss for all transferred momenta.

Since the oxygen orbitals play an important role at the O K edge, we analyze the RIXS process within the three-band Hubbard model. The photo-excited electron creates a $3d^{10}$ configuration on a neighboring copper ion. With two Cu-O hoppings (with amplitude $t_{pd}$), the $3d^{10}$ can be transferred to the other Cu ion neighboring the core hole site. To second order in $t_{pd}$, the matrix element for this process to happen is $t_{pd}^2/(\Delta + U_c)$ where $\Delta$ is the energy to transfer an electron from O to Cu and where $U_c$ is the screening potential of the core hole. After the X-ray emission at the end of the RIXS process, the two Cu spins can be left behind interchanged. The Cu L edge superexchange blocking mechanism can be neglected here, as it is of order $t_{pd}^4$. To leading order, the low energy effective spin Hamiltonian is

$$H_{\text{int}} = H_0 + (J_{\text{eff}} - J) \sum_i s_{i+\delta} s_{i+\delta}^\dagger \mathbf{S}_i \cdot \mathbf{S}_{i+2\delta} \tag{4.94}$$

with $J_{\text{eff}} = \frac{2t_{pd}^2}{\Delta + U_c}$ and where $\delta$ points from a copper to an oxygen ion. The original Heisenberg Hamiltonian $H_0$ is modified at the core hole site. Note that the Heisenberg form of the bond is preserved.

The effective scattering operator to first order in the UCL expansion is

$$\hat{O}_{\mathbf{q}} \propto \sum_i e^{i\mathbf{q}\cdot\mathbf{R}_i} \left[ \sum_{\boldsymbol{\delta}=\pm\hat{\mathbf{x}}} \epsilon_x'^* \epsilon_x e^{i\mathbf{q}\cdot\boldsymbol{\delta}} \mathbf{S}_i \cdot \mathbf{S}_{i+2\delta} + \sum_{\boldsymbol{\delta}=\pm\hat{\mathbf{y}}} \epsilon_y'^* \epsilon_y e^{i\mathbf{q}\cdot\boldsymbol{\delta}} \mathbf{S}_i \cdot \mathbf{S}_{i+2\delta} \right]. \tag{4.95}$$

In general, one would expect spectral weight at $\mathbf{q} = \mathbf{0}$ since the scattering operator does not reduce to the Hamiltonian in this case. Only when $\epsilon_x'^* \epsilon_x = \epsilon_y'^* \epsilon_y$ (and $\mathbf{q} = \mathbf{0}$) is the RIXS intensity zero.

At this point, it is instructive to make a comparison with Raman scattering. In Sec. 4.4 we established that at the Cu edges one can probe certain two-magnon modes with a definite symmetry by tuning the transferred momentum, mimicking the polarization dependence of Raman scattering. At the O K edge, however, one can also use the polarization, in addition to $\mathbf{q}$, as is clear from Eq. (4.95).

The isotropic Raman mode ($A_{1g}$) is obtained with RIXS at $\mathbf{q} = \mathbf{0}$ when $\epsilon_x'^* \epsilon_x = \epsilon_y'^* \epsilon_y$, as can be seen directly from Eq. (4.95) because the bonds are modified in an isotropic way. Indeed, the intensity should then vanish in RIXS, as noted above. The Raman $B_{1g}$ mode ($x^2$-$y^2$ symmetry) can be probed by $\mathbf{q} = \mathbf{0}$ RIXS when $\epsilon_x'^* \epsilon_x = -\epsilon_y'^* \epsilon_y$. This is the case when we transfer two units of angular momentum to the sample, *e.g.*, when $\boldsymbol{\epsilon} = (1, i, 0)$ and $\boldsymbol{\epsilon}' = (1, -i, 0)$. The Raman scattering operator for the $B_{2g}$ mode ($xy$ symmetry) vanishes for a nearest-neighbor Heisenberg antiferromagnet, which also happens in RIXS when one chooses, for instance, $\boldsymbol{\epsilon} = (1, 0, 0)$ and $\boldsymbol{\epsilon}' = (0, 1, 0)$ at $\mathbf{q} = \mathbf{0}$.

In terms of two-magnon creation processes, the general form of the RIXS scattering operator is

$$\hat{O}_{\mathbf{q}} \propto \frac{1}{N} \sum_{\mathbf{k}} \left[ \epsilon_x'^* \epsilon_x A_x + \epsilon_y'^* \epsilon_y A_y \right] \alpha_{\mathbf{k}}^\dagger \alpha_{-\mathbf{k}+\mathbf{q}}^\dagger \tag{4.96}$$

where

$$\begin{aligned} A_{x,y} = & -\cos\left(\frac{q_{x,y}}{2}\right)\left(u_{\mathbf{k}} v_{\mathbf{k}-\mathbf{q}} + u_{\mathbf{k}-\mathbf{q}} v_{\mathbf{k}}\right) + \cos\left(k_{x,y} - \frac{q_{x,y}}{2}\right) v_{\mathbf{k}} v_{\mathbf{k}-\mathbf{q}} \\ & + \frac{1}{2}\left[\cos\left(k_{x,y} - \frac{3q_{x,y}}{2}\right) + \cos\left(k_{x,y} + \frac{q_{x,y}}{2}\right)\right] u_{\mathbf{k}} u_{\mathbf{k}-\mathbf{q}}. \end{aligned} \tag{4.97}$$

One can choose to excite only half of the in-plane oxygen ions by choosing an appropriate polarization, as explained in Sec. 4.7.1. Typically, this happens for $\mathbf{q}$ directed along the [100] direction and incident $\pi$ or $\sigma$ polarization. For a scattering angle of $2\theta$, the two-magnon intensity for $\mathbf{q}$ along the [100] direction is

$$I^{(\pi)} \propto \frac{[\cos\varphi \cos(2\theta + \varphi)]^2}{N} \sum_{\mathbf{k}} A_x^2 \delta(\hbar\omega - \omega_{\mathbf{k}} - \omega_{-\mathbf{k}+\mathbf{q}}) \tag{4.98}$$

$$I^{(\sigma)} \propto \frac{1}{N} \sum_{\mathbf{k}} A_y^2 \delta(\hbar\omega - \omega_{\mathbf{k}} - \omega_{-\mathbf{k}+\mathbf{q}}) \tag{4.99}$$

for $\pi$ and $\sigma$ polarization respectively. $\varphi$ is the angle between the incident X-rays and the normal to the $CuO_2$ planes.

The results for $2\theta = 90^\circ$ are shown in Figs. 4.18 and 4.19. There is very little dispersion for either polarization. The intensity fluctuates, however, as one increases $\mathbf{q}$ or changes the polarization. The spectra are symmetric with respect to $+\mathbf{q} \leftrightarrow -\mathbf{q}$. Note that magnon-magnon interactions are not taken into account in these figures and all the following ones in this section. Magnon-magnon interactions would probably lower the energy by $\sim 25\%$, as in two-magnon Raman scattering [130]. The vanishing of the $\pi$ polarization spectra at certain $\mathbf{q}$ is due to the vanishing of the absorption amplitudes.

Note that the angle $\varphi$ is related to $\mathbf{q}$: they cannot be chosen independently. The O K edge is at an energy of around 531.2 eV [131] (and corresponding momentum of 0.269 $\hbar$Å$^{-1}$) which means that in a 90° scattering geometry one can

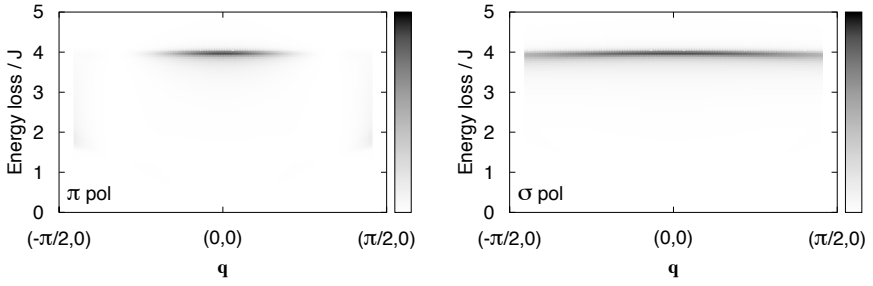


(a) (b)

**Figure 4.18:** Leading order two-magnon contribution to the O K edge RIXS spectra in 90° scattering geometry for $\mathbf{q}$ along the [100] direction with (a) incident $\pi$ polarization and (b) incident $\sigma$ polarization. The outgoing polarization is averaged over. The plots are restricted to roughly half the Brillouin zone, because this is the theoretical limit to the momentum transfer at the O K edge. The gray scales cannot be compared; for a comparison of spectral weight see Fig. 4.19(a).

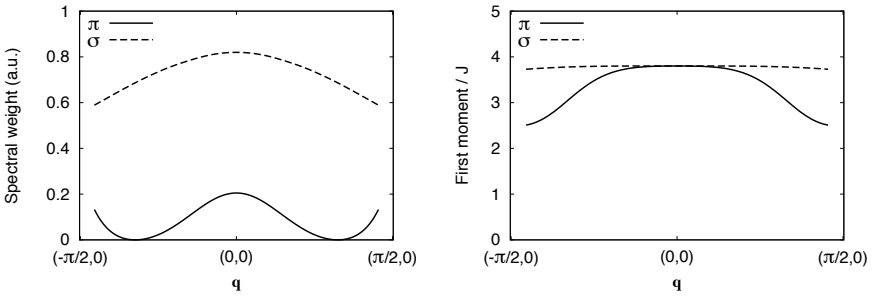


(a) (b)

**Figure 4.19:** (a) Comparison of the spectral weight of the two-magnon spectra in $\pi$ and $\sigma$ polarization along the [100] direction, obtained by integrating the spectra shown in Fig. 4.18 over energy loss. The scattering angle $2\theta = 90°$. (b) The first moment of the same spectra.

transfer a momentum of 0.380 $\hbar$Å$^{-1}$. The $(\pi, 0)$ point of the Brillouin zone is at 0.827 $\hbar$Å$^{-1}$ in $La_2CuO_4$, so one can in theory access momenta up to about 46% of the Brillouin zone boundary. In practice, when the crystal is cut parallel to the $CuO_2$ planes, it is impossible to reach more than 32% in a 90° geometry because the X-rays cannot go through the sample and its holder. (Cutting the sample in a different way circumvents this constraint [132].) This implies that the spectra of Figs. 4.18 and 4.19 cannot be probed beyond $q_x \approx \pm 0.32\pi$. These cases correspond to grazing and normal incidence, where the dipole transitions are forbidden in $\pi$ polarization, explaining the zeroes in the spectral weight. In the 90° scattering geometry, the in-plane component of $\mathbf{q}$ is $q_{\parallel} = 0.380\ \hbar$Å$^{-1} \sin(\pi/4 - \varphi)$. Grazing incidence means $q_x < 0$, and normal incidence corresponds to $q_x > 0$.

If the polarization is directed along the diagonal of the $CuO_2$ plaquettes, *i.e.*, along the [110] or [−110] direction, all oxygen ions are excited. When $\boldsymbol{\epsilon}' = \boldsymbol{\epsilon}$, the cross section is proportional to $[A_x + A_y]^2$, which is equal to the effective scattering operator of the Cu K edge when $\mathbf{q}$ is along the [110] direction. Thus, for such a geometry, the scattering intensity will vanish at $\mathbf{q} = \mathbf{0}$. However, it is currently not experimentally feasible to measure the outgoing photon's polarization. The polarization-averaged cross sections for $\mathbf{q}$ along the [110] direction are

$$I^{(\pi)} \propto \sum_{\mathbf{k}} \left( \frac{[\cos\varphi \cos(2\theta + \varphi)]^2}{4N} [A_x + A_y]^2 + \frac{\cos^2\varphi}{4N} [A_x - A_y]^2 \right) \times \delta(\hbar\omega - \omega_{\mathbf{k}} - \omega_{-\mathbf{k}+\mathbf{q}}), \tag{4.100}$$

$$I^{(\sigma)} \propto \sum_{\mathbf{k}} \left( \frac{1}{4N} [A_x + A_y]^2 + \frac{\cos^2(2\theta + \varphi)}{4N} [A_x - A_y]^2 \right) \times \delta(\hbar\omega - \omega_{\mathbf{k}} - \omega_{-\mathbf{k}+\mathbf{q}}), \tag{4.101}$$

The spectra for transferred momentum along the [110] direction in $2\theta = 90°$ scattering geometry with $\pi$ and $\sigma$ polarization are shown in Fig. 4.20, and the corresponding spectral weights and first moments are displayed in Fig. 4.21. As mentioned above, the spectra of Figs. 4.18 and 4.20 have non-zero intensity at $\mathbf{q} = \mathbf{0}$, which is very different from the Cu edges. Similar to the spectra of Fig. 4.18, there is very little dispersion. Only the intensity changes as one increases $\mathbf{q}$ or changes the polarization. A difference with the spectra along the [100] direction is the symmetry of $+\mathbf{q} \leftrightarrow -\mathbf{q}$: this symmetry is not present in the spectra along the [110] direction. At the $\Gamma$ point, a discontinuity in the spectral weight arises when the scattering plane is rotated by 45°. This becomes clear when comparing Figs. 4.19(a) and 4.21(a).

The dip in the first moment of the $\sigma$ spectrum around $\mathbf{q} = (\pi/4, \pi/4)$ in Fig. 4.21(b) is due to the $[A_x + A_y]^2$ term, which is proportional to the Cu K edge bimagnon RIXS spectrum. It is very small (but finite) at the low $\mathbf{q}$ values accessible at the O K edge. Around $\mathbf{q} = (\pi/4, \pi/4)$, the $[A_x - A_y]^2$ term is quenched and the dispersing Cu K edge bimagnon spectrum becomes visible, shifting the first moment down. For $\pi$ polarization, the spectral weight does

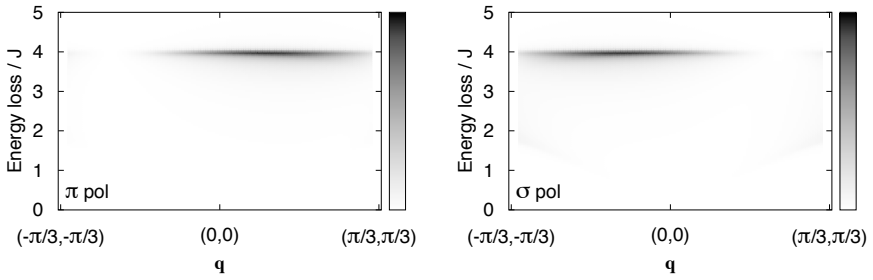


**Figure 4.20:** The two-magnon RIXS spectra at the O K edge for 90° scattering geometry and **q** along the [110] direction, with (a) incident $\pi$ polarization and (b) incident $\sigma$ polarization. The outgoing polarization is averaged over. The plots are again restricted to the theoretical limit to the transferred momentum at the O K edge. In practice, the experimental geometry limits this region even further to $|q_x| < 0.23\pi$ when the crystal is cut parallel to the $CuO_2$ planes.

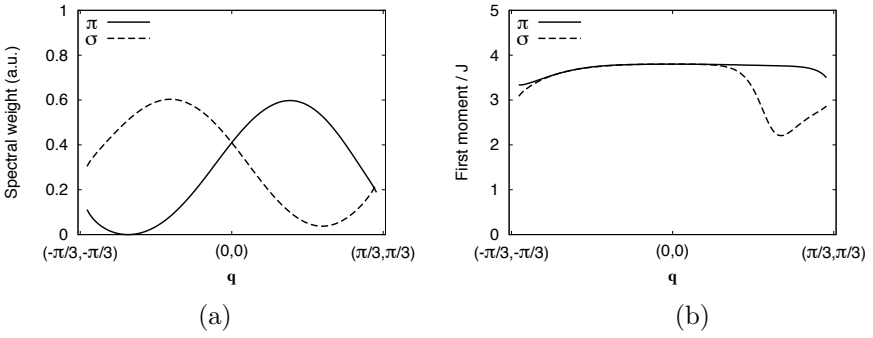


**Figure 4.21:** (a) Comparison of the spectral weight of the two-magnon spectra for **q** along the [110] direction in 90° scattering geometry, obtained by integrating the spectra shown in Fig. 4.20 over energy loss. The scale is the same as in Fig. 4.19(a). (b) The first moment of the spectra.

completely vanish at $\phi = \pi/2$ because in that case, the absorption amplitude is zero.

The RIXS experiments at the O K edge of $La_2CuO_4$ reported in Ref. [70] agree on a qualitative level with our calculations, although Bisogni *et al.* use a 110° scattering angle, while the calculations presented in this section are evaluated for a 90° geometry. In the low energy region, Bisogni *et al.* observe a broad feature ranging from 0 to 1 eV, which peaks at 500 meV and disperses downward by $\sim 50$ meV when going from the center of the Brillouin zone to $\mathbf{q} = (0.3\pi, 0.3\pi)$ or $(0.3\pi, 0)$. This small dispersion is also seen in Fig. 4.19(b). From neutron scattering, it is found that $J \approx 120$ meV [83], and with this value we reproduce the 500 meV peak and the downward dispersion of $0.7J \approx 84$ meV in $\pi$ polarization going along the [100] direction. Magnon-magnon interactions will likely make the correspondence between theory and experiment less good, as it probably decreases the theoretical peak's energy.

### 4.7.3 Other contributions to the low energy RIXS spectrum

In the experiments, the low energy spectral weight extends up to 1 eV. Any spectral weight above $\sim 0.5$ eV cannot be due to two-magnon excitations, since the two-magnon DOS is zero there. This suggests that higher order magnon excitations are also important, like four-magnon excitations.

From other work, both theoretical [82] and experimental [83], it is clear that ring exchange is quite large in the cuprates: the large numerical prefactor compensates for the smallness of the expansion parameter. At the Cu edges, ring exchange is modified or blocked by the core hole. Therefore, the effective scattering operator has a term of order $t_{pd}^8$, giving (amongst other things) four-magnon final states.

In contrast, at the O K edge, one can flip all four spins on a Néel ordered square of neighboring copper ions with only 6 hops (in the three-band Hubbard model), so the four-magnon contribution will contribute to the scattering amplitude proportional to something like $t_{pd}^6/\Delta^5$, which is in principle small, but again could have a huge prefactor because of the myriad of different ways in which the four spins can be flipped. Note that, to order $t_{pd}^6$, one only gets four-spin terms in the effective scattering operator and not in the Hamiltonian (without core hole), because the four-spin contribution to the Hamiltonian is of order $t_{pd}^8$. Therefore, one obtains a four-spin contribution at the O K edge to order $t_{pd}^6$, but not at the Cu edges. This might explain the high energy tail of the 500 meV feature.

The (non-interacting) four-magnon DOS shows a broad peak between $4J$ and $8J$ at $\mathbf{q} = \mathbf{0}$ [130]. The dispersion is minimal: the four-magnon DOS curves from all over the BZ virtually coincide. In principle it could extend from 0 to $8J$ since the single magnon energy ranges from 0 to $2J$, but as is evident, the low energy region is virtually devoid of states. Whatever the exact form of the effective

scattering operator, it is clear that the four-magnon spectrum will be 'gapped' by approximately $4J$. This value could be smaller, however: for two-magnon RIXS at the Cu edges, the low energy part of the DOS is more pronounced by the matrix elements (see Fig. 4.5). The same effect could play a role in four-magnon RIXS too.

An entirely different contribution to the O K edge might come from phonons. At the O K edge, the phonon contribution is expected to be larger than at the Cu edges because of the nature of the intermediate states. For the Cu edges, the photo-excited electron stays relatively close to the core hole: they remain on the same ion. At the O K edge, however, the core hole is on the O ion while the photo-excited electron fills the Cu 3d subshell. Because the centers of mass of the two charges are separated, there will be a relatively large attractive force between the O and the Cu ions. A strong coupling to phonons is thus expected at the O K edge.

**Acknowledgements.** We would like to thank L. Braicovich, G. Ghiringhelli, V. Bisogni and M. Moretti Sala for valuable discussions, and the ESRF, Grenoble, where part of this work was done, for its hospitality.

## 4.8 Two-magnon screening of holes in the t-J model probed by angle-resolved photoemission

Because two-magnon excitations show up so prominently in RIXS, one could ask the question if two-magnon excitations are also important in other spectroscopic techniques, or, on a more fundamental level, in the t-J model. In this section, we investigate the two-magnon screening effect on angle-resolved photoemission spectroscopy (ARPES), and calculate the contribution of two-magnon excitations to the self-energy of a hole in an antiferromagnetic background.

### 4.8.1 Introduction

It has been put forward that the t-J model, perhaps supplemented with phonons, captures the physics essential to high temperature superconductivity in cuprates. Yet understanding even the basic properties of this model is a hard task. Even the regime of very low doping of an antiferromagnet (AFM) is complicated because of the interplay between the hopping of holes and the antiferromagnetic background. The situation becomes tractable in the extreme limit of a single hole in a 2D AFM background, which has become a classic theory problem [123–125,133–141]. Experimentally, this regime can be probed with ARPES [121, 122, 142–150] and, as we will expand upon below, RIXS.

In the t-J model, the hole interacts with the spins: a moving hole rearranges the spin background, causing spin flips that correspond to single magnon excitations of the AFM. This effect is accounted for in the canonical theory approaches such as the diagrammatic self-consistent Born-approximation [123–125,133–141]. There is another channel for spin-hole scattering that is not taken into account in these approaches. A hole in an AFM reduces the number of magnetic neighbors of the surrounding spins, and these spins react to the presence of a hole. The spins thus dynamically screen any moving or static hole in the system, which is an effect that in lowest order is described by two-magnon excitations of the AFM. Precisely these two-magnon modes and their dispersions have recently been measured in the cuprates by momentum resolved RIXS at the Cu K edge [14,52,53] and possibly at the L edge too [70]. At the Cu M edge, zero momentum two-magnon excitations have been reported [15]. Describing the motion of holes in the t-J model in terms of screening by magnons only makes sense in the limit of very low doping, as magnons are not well-defined away from this limit.

The question arises how the coupling to these magnetic modes affects other physical properties. In this context we focus here on the quasiparticle (QP) excitation spectrum of the t-J model – experimentally accessible by ARPES. To this end we study theoretically the effect of the two-magnon modes on the magnetic dressing of mobile holes in the t-J model.

**ARPES.** In the limit of large $S$ the two-magnon coupling mechanism can be neglected in the t-J model, which can be seen most easily by casting the problem into a form where the hole carries spin $S - 1/2$ [124]. However, it is a priori not obvious that this argument can be extrapolated to the $S = 1/2$ limit of the high-$T_c$ cuprates, and two-magnon screening can in principle become important there. In particular one could speculate that the two-magnon coupling might be relevant in the context of a long standing challenge for theory posed by ARPES data: the width of the Zhang-Rice Singlet (ZRS) peak is broader than theory predicts. The peak width is approximately 0.3 eV at $\mathbf{k} = (\pi/2, \pi/2)$ for undoped cuprates at room temperature [142,143], increasing with temperature by $1.0 \pm 0.3$ meV/K [146,150].

This problem has attracted considerable theoretical effort [140,151–153]. Polaron formation appears to be the best candidate solution available [121,154,155]: due to the string of flipped spins left behind by a hopping hole, it is slowed down and therefore becomes more susceptible to electron-phonon interaction. The broad peak in this picture is actually the multi-phonon satellite of the quasiparticle.

In addition to contributing to slowing down the hole, the two-magnon screening of a hole in principle provides an additional mechanism to broaden the ARPES features. To settle these issues we consider the hole – two-magnon vertex quantitatively and in detail. We will first establish that the coupling of holes to two-magnon modes is independent of the hole's momentum. Subsequently we

derive the resulting self-energy of the hole, and calculate the effect of two-magnon screening on the ARPES spectra. In general, we find that the effect of this interaction is small and conclude that the two-magnon screening redistributes less than 1% of the QP spectral weight.

### 4.8.2 Two-magnon – charge interaction

**Magnetic scattering vertices.** To treat the AFM t-J model on a bipartite, inversion-symmetric lattice in the (very) low doping limit, we start from a Heisenberg model and introduce Holstein-Primakoff bosons for the magnetic degrees of freedom, see Eq. (4.11) in Sec. 4.2. When holes are introduced, they couple to the spins in two ways. First, when a hole hops from one site to another, it rearranges the spins. In an AFM background, a hopping hole creates or annihilates single magnons [123, 124, 135]. This leads to an effective reduction in the bandwidth from order $t$ to order $J$ because, loosely speaking, the hole has to wait for the relaxation of the string of energetically unfavorable spins it left behind before the hole can continue its motion [125]. In contrast, the coupling of holes to two-magnons is unrelated to the movements of a hole. Because the spins next to a hole have one less magnetic neighbor, they evolve in a different way than in an undoped AFM. In lowest order, they screen the hole with two-magnon excitations as in the screening process the $z$ component of the total spin is conserved.

To quantify the two-magnon screening, it is advantageous to introduce a virtual spin at every hole site. If all magnetic bonds that these virtual spins have with the physical spins are subsequently subtracted from the Hamiltonian, it is still possible to use Eq. (4.11) as a starting point and simply add the two-magnon coupling term

$$H_2 = -J \sum_{i,\delta} h_i^\dagger h_i \mathbf{S}_i \cdot \mathbf{S}_{i+\delta}, \tag{4.102}$$

where $h_i^{(\dagger)}$ is the hole annihilation (creation) operator, and $\delta$ points to nearest neighbors. We assume for simplicity that holes are surrounded only by spins, which is reasonable at low doping and certainly true for a single hole in undoped cuprates, as one encounters in the RIXS intermediate state. $H_2$ does not commute with $H_0$. Rewriting $H_2$ in terms of magnon operators at the linear spin wave level, one arrives at

$$\begin{aligned} H_2 = &\sum_{\mathbf{k},\mathbf{p},\mathbf{l}} g_{\mathbf{k},\mathbf{p}} h^\dagger_{\mathbf{l}-\mathbf{k}-\mathbf{p}} h_{\mathbf{l}} (\alpha^\dagger_{\mathbf{k}} \alpha^\dagger_{\mathbf{p}} + \alpha_{-\mathbf{k}} \alpha_{-\mathbf{p}}) + \sum_{\mathbf{k},\mathbf{p},\mathbf{l}} f_{\mathbf{k},\mathbf{p}} h^\dagger_{\mathbf{l}-\mathbf{k}-\mathbf{p}} h_{\mathbf{l}} \alpha^\dagger_{\mathbf{k}} \alpha_{-\mathbf{p}} \\ &+ \sum_{\mathbf{l}} h^\dagger_{\mathbf{l}} h_{\mathbf{l}} \left[ zJS^2 - \frac{1}{N} \sum_{\mathbf{k}} (\omega_{\mathbf{k}} - zJS) \right], \end{aligned} \tag{4.103}$$

with vertices

$$f_{\mathbf{k},\mathbf{p}} = -\frac{zJS}{N}\left[(1+\gamma_{\mathbf{k}+\mathbf{p}})(u_{\mathbf{k}}u_{\mathbf{p}}+v_{\mathbf{k}}v_{\mathbf{p}})-(\gamma_{\mathbf{k}}+\gamma_{\mathbf{p}})(u_{\mathbf{k}}v_{\mathbf{p}}+v_{\mathbf{k}}u_{\mathbf{p}})\right], \quad (4.104)$$

$$g_{\mathbf{k},\mathbf{p}} = +\frac{zJS}{2N}\left[(1+\gamma_{\mathbf{k}+\mathbf{p}})(u_{\mathbf{k}}v_{\mathbf{p}}+v_{\mathbf{k}}u_{\mathbf{p}})-(\gamma_{\mathbf{k}}+\gamma_{\mathbf{p}})(u_{\mathbf{k}}u_{\mathbf{p}}+v_{\mathbf{k}}v_{\mathbf{p}})\right]. \quad (4.105)$$

The vertices are independent of the hole momentum, and symmetric under the exchange of the magnon momenta $\mathbf{k}$ and $\mathbf{p}$. Furthermore, because of energy and momentum conservation for a hole producing two magnons, $g_{\mathbf{k},-\mathbf{k}} = 0$. The last term in Eq. (4.103) corresponds to the energy cost of breaking $z$ magnetic bonds in the classical Néel state, plus quantum corrections from linear spin wave theory. It cancels the contribution of the unphysical spins to the constant in Eq. (4.11).

Although $H_2$ has no intrinsically small parameter, it will turn out that its effects are in all respects quite small. This comes about because of the Bogoliubov coefficients $u_{\mathbf{k}}$ and $v_{\mathbf{k}}$ that make $f_{\mathbf{k},\mathbf{p}}$ and $g_{\mathbf{k},\mathbf{p}}$ in general small. At the only momenta for which $u_{\mathbf{k}}$ and $v_{\mathbf{k}}$ diverge, *i.e.*, $\mathbf{k} = (0,0)$ and $\mathbf{k} = (\pi,\pi)$, the number of available magnon states is so small that processes involving the low energy magnons at these wave vectors do not contribute much to the hole's self-energy in the thermodynamic limit. This observation justifies a perturbation approach.

**Hole self-energy and spectral function.** In the following we calculate the loewst order contribution of two-magnon screening processes to the QP self-energy. The dispersion of the propagating hole is renormalized by single-magnon excitations, and the QP energy is $\sum_{\mathbf{k}} \epsilon_{\mathbf{k}} h^\dagger_{\mathbf{k}} h_{\mathbf{k}}$. The effective dispersion $\epsilon_{\mathbf{k}}$ can be obtained from a variational analysis [125] extended with (effective) second and third neighbor hopping [156], so that

$$\begin{aligned}\epsilon_{\mathbf{k}} = {} & 4t'\cos k_x \cos k_y + 2t''(\cos 2k_x + \cos 2k_y) \\ & - \sqrt{0.44J^2 + t^2\{4.56 - 0.70(\cos k_x + \cos k_y)^2\}} + \text{const.}\end{aligned} \quad (4.106)$$

where the constant is chosen such that the minimum of $\epsilon_{\mathbf{k}}$ is 0. Further, we take $t = 3.1J$, $t' = -0.36J$, $t'' = 0.18J$ to get a best fit to data on the Mott insulator $Sr_2CuO_2Cl_2$ [142, 153]. $\epsilon_{\mathbf{k}}$ is consistent with the effective QP dispersion derived in Ref. [153].

The lowest order self-energy diagram of the QP at zero temperature due to interaction with two-magnon modes is shown in Fig. 4.22(a). Expanding $g_{\mathbf{k},\mathbf{p}}$ around the singular points $\mathbf{k} \to \mathbf{0}, \boldsymbol{\pi}$ [with $\mathbf{0} = (0,0)$ and $\boldsymbol{\pi} = (\pi,\pi)$], we find that $g_{\mathbf{0},\mathbf{0}} = g_{\boldsymbol{\pi},\mathbf{0}} = g_{\boldsymbol{\pi},\boldsymbol{\pi}} \to 0$, so the holes do not couple to long wavelength magnons via $H_2$, regardless of the hole dispersion. Consequently, two-magnon broadening of the QP peak around the bottom of the band will vanish because of a lack of decay processes. To compute the two-magnon contribution to the QP

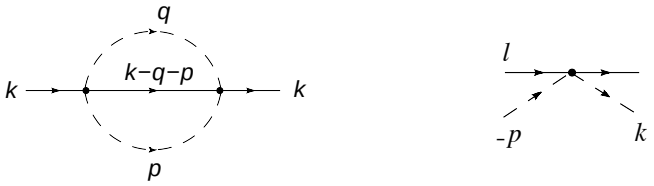


**Figure 4.22:** (a) Self-energy diagram for two-magnon screening of a hole with momentum $\mathbf{k}$. The solid lines represent the hole, the dashed lines represent magnons. The vertices indicate an interaction via the $g_{\mathbf{k},\mathbf{p}}$ term of Eq. (4.103). (b) At finite temperatures, long wavelength magnons are present in the system and they can scatter off the holes via the $f_{\mathbf{k},\mathbf{p}}$ term, increasing their linewidth.

self-energy we introduce the hole and magnon Green's functions, respectively, as

$$G(\mathbf{k}, t-t') = -i \left\langle \psi_0 \right| T\{h_{\mathbf{k}}(t) h^{\dagger}_{\mathbf{k}}(t')\} \left| \psi_0 \right\rangle , \tag{4.107}$$

$$D(\mathbf{k}, t-t') = -i \left\langle \psi_0 \right| T\{\alpha_{\mathbf{k}}(t) \alpha^{\dagger}_{\mathbf{k}}(t')\} \left| \psi_0 \right\rangle \tag{4.108}$$

where $|\psi_0\rangle$ is the ground state of the perturbed system. The unperturbed Green's functions are

$$D^{(0)}(\mathbf{k}, \omega) = \int_{-\infty}^{\infty} dt \; e^{i\omega t} D^{(0)}(\mathbf{k}, t) = \frac{1}{\omega - \omega_{\mathbf{k}} + i\eta}, \tag{4.109}$$

$$G^{(0)}(\mathbf{k}, \omega) = \int_{-\infty}^{\infty} dt \; e^{i\omega t} G^{(0)}(\mathbf{k}, t) = \frac{1}{\omega - \epsilon_{\mathbf{k}} + i\eta}, \tag{4.110}$$

where $\eta$ is a (very small) convergence factor. When the perturbation $H_2$ is turned on, the hole Green's function acquires a self-energy:

$$G(\mathbf{k}, \omega) = \frac{1}{\omega - \epsilon_{\mathbf{k}} - \Sigma(\mathbf{k}, \omega) + i\eta}. \tag{4.111}$$

To second order in the interaction, the self-energy diagram, shown in Fig. 4.22(a), is

$$\Sigma^{(2)}(\mathbf{k}, \omega) = \sum_{\mathbf{p},\mathbf{q}} \frac{2 g^2_{\mathbf{p},\mathbf{q}}}{\omega - \omega_{\mathbf{p}} - \omega_{\mathbf{q}} - \epsilon_{\mathbf{k}-\mathbf{p}-\mathbf{q}} + i\eta}. \tag{4.112}$$

The hole spectral function is by definition

$$A(\mathbf{k}, \omega) = -\frac{1}{\pi} \mathfrak{Im}\{G(\mathbf{k}, \omega)\} = \frac{1}{\pi} \frac{|\mathfrak{Im}\{\Sigma\}|}{(\omega - \epsilon_{\mathbf{k}} - \mathfrak{Re}\{\Sigma\})^2 + |\mathfrak{Im}\{\Sigma\}|^2}. \tag{4.113}$$

We evaluated the QP spectral function within the formalism above and the result is shown in Fig. 4.23. From the bottom two figures showing the spectrum

with the second order self-energy, it can be seen that the QP broadening due to two-magnon screening is below about $0.1J \approx 12$ meV. For more broadening at momenta away from $(\pi/2, \pi/2)$, the bare hole dispersion would have to reach higher energies, around $4J$, where the two-magnon DOS is highest and thus the number of decay channels is maximized. This observation is reflected in $\mathfrak{Im}\{\Sigma^{(2)}\}$ peaking in this region to about $-0.12J$, broadening the peak just a little more.

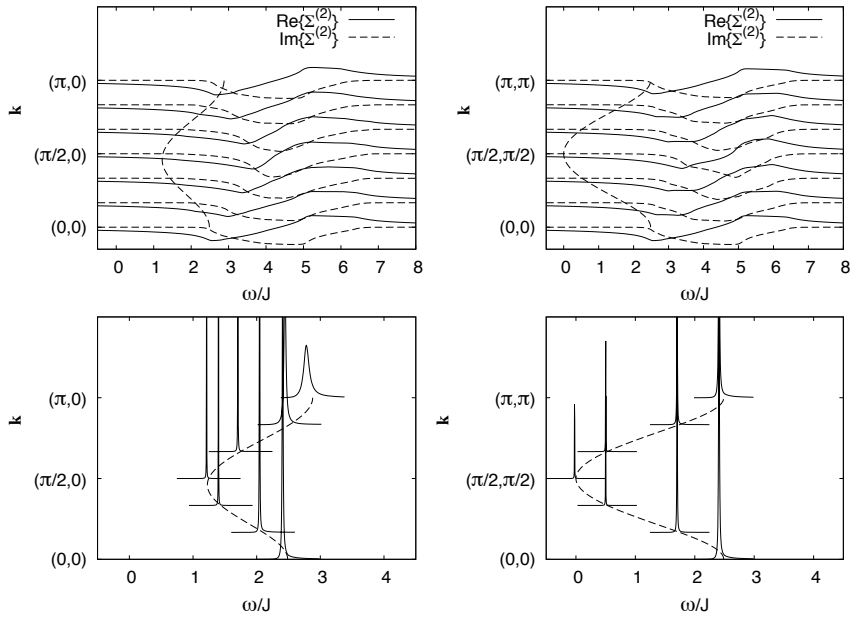


**Figure 4.23:** Hole self-energy to second order in $H_2$ (top figures) and the corresponding spectra (bottom figures). In the top figures, the solid line represents the real part of $\Sigma^{(2)}$, while the dashed line represents the imaginary part. The left figures show $\mathbf{k}$ ranging from $(0,0)$ to $(\pi,0)$, while the right figures show $(0,0)$ to $(\pi,\pi)$. The dashed gray lines indicate the bare hole dispersion (4.106). A tiny artificial broadening of $0.02J$ is introduced for the numerical evaluation of the spectra. Around $(\pi/2,\pi/2)$, the spectrum approaches a delta function; their height is artificially limited due to the finite energy resolution of the numerical evaluation of the spectra.

Although the zero temperature mechanism we considered above does not explain the ARPES ZRS peak broadening, we can also consider finite temperature effects, where the coupling $f_{\mathbf{k},\mathbf{p}}$ becomes important. At non-zero temperatures, low energy magnons are present in the system and they can scatter off the holes via the vertex $f_{\mathbf{k},\mathbf{p}}$, as shown in Fig. 4.22(b). This decreases the lifetime of the quasiparticles. Holes at the bottom of the band can only scatter the low energy magnons into other low energy modes because of energy conservation.

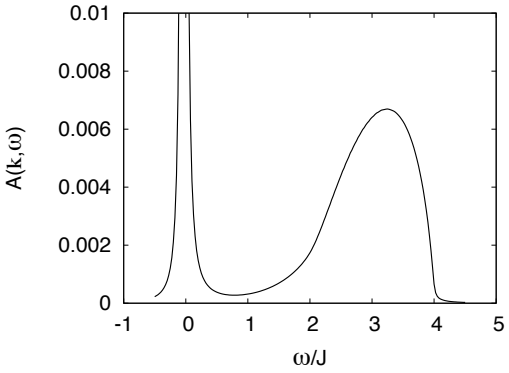


**Figure 4.24:** The spectrum of a static, two-magnon screened hole. The spectrum is independent of the hole's momentum. It consists of a sharp quasiparticle peak at $\omega \approx 0$ and a two-magnon incoherent feature at $\omega \approx 2 - 4J$.

By expanding $f_{\mathbf{k},\mathbf{p}}$ around the singular points at the center and corners of the BZ, we see that $f_{\mathbf{0},\mathbf{0}} = f_{\boldsymbol{\pi},\mathbf{0}} = f_{\boldsymbol{\pi},\boldsymbol{\pi}} \to 0$, and the amplitude for this kind of scattering process vanishes. We conclude that, even if low energy magnons are present at finite temperatures, the lifetime of quasiparticles near the bottom of the band does not increase due to single magnon scattering via $H_2$, and the zero temperature results are robust with respect to finite temperature effects.

To make a connection with RIXS at the Cu L edge, we calculate the spectrum for a flat band $\epsilon_{\mathbf{k}} \to$ const. This situation corresponds to RIXS since to good approximation the intermediate state is excitonic [157]: the $3d^{10}$ configuration is bound to the local core hole, and its dispersion is zero. Then, $\Sigma^{(2)}$ is independent of $\mathbf{k}$, and so is the spectrum $A(\mathbf{k}, \omega)$. The resulting spectrum is shown in Fig. 4.24.

As is clear from Fig. 4.24, the two-magnon satellite between $J$ and $4J$ carries approximately 1.1% of the total spectral weight. At first glance this small number might be surprising, considering that the two-magnon excitations appear so strongly in RIXS, particularly at the K edge [14, 52, 53]. We first note that in RIXS the elastic signal is (largely) pushed to the Bragg peaks and in that sense the dominating quasiparticle peak of Fig. 4.24 is absent. This argument is of course heuristic because the RIXS cross section is not directly related to the single particle spectral function $A(\mathbf{k}, \omega)$, but rather given by the Kramers-Heisenberg relation (2.30). Also, at the Cu L edge, the two-magnon peak seems to be quite small compared to other magnetic features [11], which is at least qualitatively agreeing with the theoretical result presented here. It might be due to the absence of any other spectral weight that two-magnon excitations are seen so clearly in Cu K edge RIXS.

### 4.8.3 Conclusions

We conclude that the two-magnon screening of holes in the t-J model is a very small effect. It is by far not enough to explain the broad ARPES peaks: two-magnon screening gives a broadening of at most $0.1J \approx 12$ meV, while experimentally the peaks have a broadening of 0.3 eV. Earlier work [140] has already

excluded broadening due to single magnon processes, and our results are in agreement with Ref. [143], which states that the ZRS peak broadening is probably not due to interactions with the Cu spins. Their reasoning is that at certain momenta, ARPES ejects O 2p electrons from the sample that, by symmetry, do not hybridize with the magnetic Cu ions. These ARPES peaks have exactly the same low energy line shape as the ZRS peaks that do communicate with the Cu ions. The authors therefore assume that the ZRS too owes it lineshape not to the Cu spins, but to something else.

The calculations for a dispersionless hole indicate that two-magnon excitations should show up only weakly in RIXS processes with a $3d^{10}$ intermediate state: we expect two-magnon excitations to be some two orders of magnitude smaller in intensity than direct RIXS processes that lead to the elastic line, single magnons and dd excitations. That a two-magnon signal is observed at the Cu K and L edges illustrates how sensitive RIXS is becoming [11, 14, 53].

### 4.8.4 Acknowledgements

We thank George Sawatzky, Byron Freelon and Tom Devereaux for fruitful discussions. This work is supported by the U.S. Department of Energy, Office of Basic Energy Sciences under contract DE-AC02-76SF00515 and benefited from the RIXS collaboration supported by the Computational Materials Science Network (CMSN) program under grant number DE-FG02-08ER46540. This work is supported by the Dutch 'Stichting voor Fundamenteel Onderzoek der Materie (FOM)'.